THE SANTA BARBARA CLUSTER COMPARISON PROJECT: A COMPARISON OF COSMOLOGICAL HYDRODYNAMICS SOLUTIONS

C. S. FRENK,[1] S. D. M. WHITE,[2] P. BODE,[3] J. R. BOND,[4] G. L. BRYAN,[5] R. CEN,[6] H. M. P. COUCHMAN,[7] A. E. EVRARD,[8] N. GNEDIN,[9] A. JENKINS,[1] A. M. KHOKHLOV,[10] A. KLYPIN,[11] J. F. NAVARRO,[12] M. L. NORMAN,[13,14] J. P. OSTRIKER,[6] J. M. OWEN,[15,16] F. R. PEARCE,[1] U.-L. PEN,[17] M. STEINMETZ,[18] P. A. THOMAS,[19] J. V. VILLUMSEN,[2] J. W. WADSLEY,[4] M. S. WARREN,[20] G. XU,[21] AND G. YEPES[22]

ABSTRACT

We have simulated the formation of an X-ray cluster in a cold dark matter universe using 12 different codes. The codes span the range of numerical techniques and implementations currently in use, including smoothed particle hydrodynamics (SPH) and grid methods with fixed, deformable, or multilevel meshes. The goal of this comparison is to assess the reliability of cosmological gasdynamical simulations of clusters in the simplest astrophysically relevant case, that in which the gas is assumed to be nonradiative. We compare images of the cluster at different epochs, global properties such as mass, temperature and X-ray luminosity, and radial profiles of various dynamical and thermodynamical quantities. On the whole, the agreement among the various simulations is gratifying, although a number of discrepancies exist. Agreement is best for properties of the dark matter and worst for the total X-ray luminosity. Even in this case, simulations that adequately resolve the core radius of the gas distribution predict total X-ray luminosities that agree to within a factor of 2. Other quantities are reproduced to much higher accuracy. For example, the temperature and gas mass fraction within the virial radius agree to within about 10%, and the ratio of specific dark matter kinetic to gas thermal energies agree to within about 5%. Various factors, including differences in the internal timing of the simulations, contribute to the spread in calculated cluster properties. Based on the overall consistency of results, we discuss a number of general properties of the cluster we have modeled.

Subject headings: cosmology: theory — dark matter — galaxies: clusters: general — large-scale structure of universe — X-rays: galaxies

1. INTRODUCTION

Computer simulations have played a central role in modern cosmology. Two decades after the first cosmological simulations were performed, this technique is firmly established as the main theoretical tool for studying the nonlinear phases of the evolution of cosmic structure and for testing theories of the early universe against observational data.

The first generation of cosmological simulations employed *N*-body techniques to follow the clustering evolution of a dissipationless dark matter component. This approach proved powerful enough to reject the idea that the dark matter consists of massive neutrinos and to establish the viability of the alternative hypothesis that the dark matter is made up of cold collisionless particles. In the last decade, *N*-body techniques have been further refined and applied to a wide range of cosmological problems. *N*-body simulations are now sufficiently well understood that the validity of analytic approximations is often gauged by reference to simulation results.

[1] Department of Physics, University of Durham, DH1 3LE, England.

[2] Max-Planck-Institut für Astrophysik, Karl Schwarzschild Strasse 1, D-85740 Garching bei München, Germany.

[3] Department of Physics and Astronomy, University of Pennsylvania, 33d and Walnut Streets, Philadelphia, PA 19104-6396.

[4] Canadian Institute for Theoretical Astrophysics and Department of Astronomy, University of Toronto, 60 George Street, Toronto ON M5S 3H8, Canada.

[5] Department of Physics, Massachusetts Institute of Technology, Cambridge, MA 02139.

[6] Princeton University Observatory, Princeton, NJ 08544.

[7] Department of Physics and Astronomy, University of Western Ontario, London, Ontario N6A 3K7, Canada.

[8] Department of Physics, University of Michigan, Ann Arbor, MI 48109-1120.

[9] Department of Astronomy, University of California, Berkeley, Berkeley, CA 94720.

[10] Laboratory for Computational Physics and Fluid Dynamics, Code 6404, Naval Research Laboratory, Washington, DC, 20375.

[11] Department of Astronomy, New Mexico State University, Las Cruces, NM 88001.

[12] Department of Physics and Astronomy, University of Victoria, Victoria, BC, V8W 2P6, Canada.

[13] Laboratory for Computational Astrophysics, NCSA, University of Illinois at Urbana-Champaign, 405 North Mathews Avenue, Urbana, IL 61801.

[14] Department of Astronomy, University of Illinois at Urbana-Champaign, 1002 West Green Street, Urbana, IL 61801.

[15] Department of Astronomy, Ohio State University, Columbus, OH 43210.

[16] Lawrence Livermore National Laboratory, L-312, Livermore, CA 94550.

[17] Harvard-Smithsonian Center for Astrophysics, 60 Garden Street, Cambridge, MA 02138.

[18] Steward Observatory, University of Arizona, Tucson, AZ 85721.

[19] Chemistry, Physics, and Environmental Sciences, University of Sussex, Falmer, Brighton BN1 9QH, UK.

[20] Theoretical Astrophysics, T-6, Mail Stop B288, Los Alamos National Laboratory, Los Alamos, NM 87545.

[21] Board of Studies in Astronomy and Astrophysics, University of California, Santa Cruz, Santa Cruz, CA 95064.

[22] Departamento de Física Teórica C-XI, Universidad Autónoma de Madrid, Cantoblanco 28049, Madrid, Spain.

The main limitation of N-body techniques is, of course, that they are relevant only to the evolution of dark matter. In order to model the visible universe, it is necessary to include additional physical processes. First, it is necessary to model a gas component that is gravitationally coupled to the dark matter. In the simplest case, the gas may be assumed to be nonradiative. Although still highly simplified, this case has immediate applications in the study of the hot plasma in galaxy clusters. At the next level of complexity, heating and cooling processes must be included. This is required, for example, to investigate the physical properties of the gas clouds responsible for QSO absorption lines. Additional processes, such as star formation and the associated feedback of energy and mass, are necessary to model galaxy formation.

Since the late 1980s a variety of techniques have been developed to simulate gasdynamics and related processes in a cosmological context. In part inspired by the success of the N-body program, the first gasdynamical techniques were based on a particle representation of Lagrangian gas elements using the smoothed particle hydrodynamics (SPH) technique (Lucy 1977; Gingold & Monaghan 1977; Evrard 1988). Soon thereafter, fixed-mesh Eulerian methods were adapted (Cen et al. 1990; Cen 1992) and, more recently, Eulerian methods with submeshing (Bryan & Norman 1995) or deformable moving meshes (Gnedin 1995; Pen 1995, 1998) have been developed, as well as extensions of the SPH technique (Shapiro et al. 1996). These codes are actively being applied to a variety of cosmological problems, ranging from the formation of individual galaxies and galaxy clusters to the evolution of Lyα forest clouds and the large-scale galaxy distribution.

Because of the inherent complexity of gasdynamics in a cosmological context, such simulations are more difficult to validate than N-body simulations. Standard test cases with known analytical solutions (such as shock tubes) are far removed from the conditions prevailing in cosmological situations where the gas is coupled to dark matter, and this, in turn, evolves through a hierarchy of mergers. The closest analogue to a realistic cosmological problem is the Bertschinger (1985) solution for the collapse of a spherical cluster. Although this model provides a useful test of numerical hydrodynamics implementations, it ignores the merging processes that are a dominant aspect of the formation of realistic clusters. In general, the strongly nonlinear and asymmetric nature of gravitational evolution in a cosmological context differs greatly from the regime that can be studied analytically or in laboratory experiments.

In this paper we carry out an exercise intended as a step toward assessing the reliability of current numerical studies of cosmological gasdynamics. We address one of the simplest astrophysically relevant problems, the formation of a large cluster in a hierarchical cold dark matter (CDM) model, using a variety of codes that span the entire range of numerical techniques in use today. The cluster problem is relatively simple because, except in the inner parts, the cooling time of the gas exceeds the age of the universe and so, to a good approximation, the gas may be treated as nonradiative.

The aim of this exercise is to assess the extent to which existing modeling techniques give consistent and reproducible results in a realistic astrophysical application. Our comparison is, by design, quite general. We simply specify the initial conditions for the formation of a cluster and let different simulators approach the problem in the manner they regard as most appropriate. Our comparison therefore encompasses not only the hydrodynamics simulation techniques themselves but also individual choices of boundary conditions, resolution, internal variables such as the integration time steps, and even the definition of cluster center. We are therefore able to address issues such as the reproducibility of the X-ray luminosity and surface brightness of simulated clusters. It is not our intention to test the accuracy of any individual code: all the codes used in this paper have already been extensively tested against known analytic solutions. An earlier comparison of a subset of the techniques considered here was presented by Kang et al. (1994b). These authors simulated a large cosmological volume and focused on statistical properties of the large-scale structure, rather than on the nonlinear properties of an individual cluster that concern us here.

This project was initiated as part of the activities of the program, "Cosmic Radiation Backgrounds and the Formation of Galaxies," which took place at the Institute for Theoretical Physics in Santa Barbara in 1995. Most active groups in the field of cosmological hydrodynamics simulations agreed to participate. Initial conditions for the cluster simulation were set up as described in § 2. The codes used in the comparison are briefly described in § 3. Participants were asked to analyze their results with a suite of predefined diagnostics, including images, global properties such as mass and X-ray luminosity, and radial profiles of the dark matter density, gas density, temperature, etc. The images and a comparison of quantitative results are given in § 4. Our paper concludes in § 5 with a summary and discussion of results, including some general conclusions regarding the properties of the simulated cluster.

2. THE SIMULATION

We simulated the formation of a galaxy cluster in a flat CDM universe. The initial fluctuation spectrum was taken to have an asymptotic spectral index, $n = 1$, and shape parameter, $\Gamma = 0.25$, the value suggested by observations of large-scale structure (e.g., Efstathiou, Bond, & White 1992). The cosmological parameters assumed were $\Omega = 1$ for the mean density; $H_0 = 50$ km s^{-1} Mpc^{-1} for the Hubble constant; $\sigma_8 = 0.9$ for the present-day linear rms mass fluctuation in spherical top hat spheres of radius 16 Mpc; and $\Omega_b = 0.1$ for the baryon density (in units of the critical density).

2.1. Initial Conditions

Initial conditions were laid down using the constrained Gaussian random field algorithm of Hoffman & Ribak (1991). The cluster perturbation was chosen to correspond to a 3 σ peak of the density field smoothed with a Gaussian filter of radius $r_0 = 10$ Mpc (in exp $[-0.5(r/r_0)^2]$). The perturbation was centered on a cubic region of side $L = 64$ Mpc. We used the fit to the CDM transfer function given by equation (G3) of Bardeen et al. (1986) and recommended a starting epoch of $z = 20$.

To offer flexibility, the initial conditions were generated at very high resolution. Two alternative forms were supplied:

1. the dimensionless linear $\delta\rho/\rho$ field (normalized to the present), tabulated on a 256^3 cubic mesh;
2. the linear theory displacements for 256^3 points on a cubic mesh.

The initial conditions were generated by Shaun Cole. These are publicly available on the Internet[23] or by request from C. S. F.

2.2. Simulation Diagnostics

The simulation data were output at redshifts $z = 8, 4, 2, 1, 0.5$, and 0, and the following properties were calculated.

1. *Images.*—At each epoch, two-dimensional images of various quantities in the central $(32 \text{ Mpc})^3$ comoving volume were generated. The quantity of interest was projected along the z-axis, smoothed as specified below, and tabulated on a 1024^2 mesh. Two smoothings were employed:

a) a Gaussian smoothing with kernel, $\exp[-0.5(r/r_0)^2]$, at a fixed resolution of $r_0 = 250$ kpc (comoving);

b) a smoothing of choice, as determined by each simulator.

The first set of images was used for a uniform comparison of all the models, while the second set was supplied in order to display the results of each technique in the best possible light.

Images of the following quantities were made:

a) the projected dark matter density (in $M_\odot \text{ Mpc}^{-2}$);

b) the projected gas density (in $M_\odot \text{ Mpc}^{-2}$);

c) the X-ray surface brightness, $\int \mathcal{L}_X \, dl$ (X-ray emissivities per unit volume were calculated as $\mathcal{L}_X = \rho^2 T^{1/2}$, with ρ in $M_\odot \text{ Mpc}^{-3}$ and T in K);

d) the emission-weighted temperature ($\int \mathcal{L}_X T \, dl / \int \mathcal{L}_X \, dl$).

2. *Global properties.*—We defined the cluster to be the mass contained inside a sphere of radius r_{200}, such that the mean interior overdensity is 200. The following global properties of the cluster were then computed at $z = 0$:

a) the value of r_{200};

b) M_{dm}, the total dark matter mass (in $M_\odot$);

c) V_{dm}, the rms velocity of dark matter particles (in km s^{-1});

d) M_{gas}, the total gas mass (in $M_\odot$);

e) $\overline{T}$, the mean (mass-weighted) temperature (in K);

f) U, the total bulk kinetic energy of the gas (in ergs);

g) $L_{\text{tot}} = \int_0^{r_{200}} \mathcal{L}_X \, dV$ ($\mathcal{L}_X$ units as above; V in Mpc^3);

h) $\mathcal{I} = \sum_i m_i x_i x_i / \sum_i m_i$, the inertia tensor for dark matter and gas (in Mpc^2).

Radial profiles.—In 15 spherical shells of logarithmic width 0.2 dex and inner radii 10 kpc $\leq r < 10$ Mpc, the following quantities were obtained:

a) $\rho_{\text{dm}}(r)$, the dark matter density profile (in $M_\odot \text{ Mpc}^{-3}$);

b) $\sigma_{\text{dm}}(r)$, the dark matter velocity dispersion profile (in km s^{-1});

c) $\rho_{\text{gas}}(r)$, the gas density profile (in $M_\odot \text{ Mpc}^{-3}$);

d) $T(r)$, the mass-weighted gas temperature profile (in K);

e) $\mathcal{L}_X(r)$, the "X-ray luminosity" profile calculated as the total luminosity in each bin, divided by its volume (in units as above).

Each simulator was provided with the two initial conditions files and the list of required diagnostics (in a prespeci-

fied format). Everything else was left to the discretion of each simulator including, for example, the definition of the cluster center. All data were sent directly to the organizers (C. S. F. and S. D. M. W.), and participants were strongly discouraged from private intercomparison of results. A surprising number of iterations was required to obtain consistent outputs in a single set of units and formats.

Wadsley joined the project after the original deadline had expired and the first set of results was known. Discrepancies in a preliminary comparison of results led Gnedin to revise his code and resubmit a new simulation. Bryan's stated spatial resolution was changed from 80 to 30 kpc after preliminary comparison suggested that he had been too pessimistic in stating his resolution.

3. THE CODES

The numerical codes used for this project employ a variety of techniques to solve the evolution equations for a two-component fluid of dark matter and nonradiative gas coupled by gravity. In what follows, each code is identified by the name of the author who was primarily responsible for carrying out each simulation. The codes are of two general types: SPH and grid-based. SPH simulations were carried out by Couchman, Evrard, Jenkins, Navarro, Owen, Steinmetz, and Wadsley. The simulations by Couchman and Jenkins used the same basic code (HYDRA), the serial version in the former case and a parallel version in the latter. (These two simulations were done independently and used different numbers of particles and different values for the simulation parameters: gravitational softening, smoothing length, time step, etc.) Owen's code differs from the others in the use of an anisotropic SPH kernel. The grid-based methods employ either a single, fixed mesh (Cen, Yepes), a two-level multimesh (Bryan), or a deformable mesh (Gnedin, Pen). Warren carried out a high-resolution simulation of the evolution of the dark matter only.

A brief description of each code follows, together with references in which the reader may find a fuller discussion of techniques and the tests to which each code has been subjected. Details of each simulation are given in Table 1.

3.1. SPH Codes

3.1.1. Couchman & Thomas: Hydra (Adaptive P^3M-SPH)

Hydra is functionally equivalent to the standard particle-particle-particle-mesh, N-body–SPH (P^3M-SPH) implementation, but with the automatic placement of a hierarchy of refined meshes in regions of high particle density. This avoids the dramatic performance degradation caused by the direct summation (PP) component of standard P^3M codes under heavy particle clustering. In the present simulation, at a redshift of $z = 0.5$, the CPU time per step had increased by a factor of 4.5 from the essentially uniform initial conditions at $z = 49$ and remained at this level to the end of the simulation. A maximum of four levels of mesh refinement was chosen by the code.

The code automatically chooses a global time step to ensure accurate time integration. This value is determined by the maximum instantaneous values of particle velocities and accelerations of both gas and dark matter particles. An optimal low-order integration scheme is used for advancing particle positions and velocities. Full details of the code are available in Couchman, Thomas, & Pearce (1995), and the source code may be found in Couchman, Pearce, & Thomas (1996).

[23] Available at http://star-www.dur.ac.uk/ csf/clusdata/.

TABLE 1
SIMULATION DETAILS

Name (1)	Code (2)	Reference for Code (3)	h (kpc) (4)	M_{dm} ($10^{10}\,M_\odot$) (5)	M_{gas} ($10^9\,M_\odot$) (6)	ϵ (kpc) (7)	Δt_{min} (8)	Δt_{ave} (9)	N_{res} (10)	Image Smoothing (11)	Computer (12)	T_{cpu} (hr) (13)	Memory (Mbyte) (14)	Date (15)
Bryan	SAMR	1	15	0.78	...	30	1/4000	1/1000	3.3×10^5	Adaptive $2h$	SGI Pow. Ch.	200	500	1996 Mar
Cen	TVD	2	125	0.10	...	312	1/660	1/660	36751	Gaussian 200 kpc	IBM SP2	5312	4400	1996 Jan
Couchman...	Hydra	3	40	6.25	6.94	40	1/2500	1/1826	15291	Adaptive $1h$	DEC Alpha 250 MHz	77.3	95	1995 Dec
Evrard	P³M-SPH	4	53	6.25	6.94	75	1/4000	1/4000	15571	Adaptive $3.5h$	HP735	320	16.5	1996 Jan
Gnedin.......	SLH-P³M	5	100	6.25	6.94	100	1/4096	1/2315	1.5×10^5	Gaussian 100 kpc	SGI Pow. Ch.	136	90	1997 Sep
Jenkins.......	Par. Hydra	6	20	0.78	0.87	20	1/20000	1/4489	2.5×10^5	Adaptive	Cray-T3D	5000	512	1996 Apr
Navarro	Grape+SPH	7	30	6.18	6.87	30	1/26074	1/651	13700	Gaussian 30 kpc	Sparc10 + GRAPE-3AF	120	75	1996 Apr
Owen	ASPH	8	300	50	55.5	250	1/133713	1/980	1691	Adaptive	Cray-YMP/4E	40	106	1996 Mar
Pen	MMH	9	50	0.10	0.87	45	1/3523	1/1630	88953	Adaptive	SGI Pow. Ch.	480	900	1996 Apr
Steinmetz....	GrapeSPH	10	50	6.25	6.94	25	1/7267	1/6500	14876	Adaptive	Sparc10 + GRAPE-3AF	28	22	1996 Apr
Wadsley	P³MG-SPH	11	33.7	6.25	6.94	24	1/4496	1/1630	15918	Adaptive $h \geq 40$ kpc	DEC Alpha EV5	119	100	1996 Jul
Warren	Tree	12	5	0.11	...	5	1/2550	1/2550	...	Adaptive	Intel-Delta	15360	1000	1996 Apr
Yepes	PM-FCT	13	400	0.45	...	960	1/15000	1/6364	1024	None	Cray-YMP	350	480	1995 Nov

NOTE.—Col. (1): Name of principal simulator; col. (2): name of code; col. (3): reference for code description; col. (4): spatial resolution for gas at cluster center (cell size or smoothing length of SPH kernel); col. (5): dark matter particle mass; col. (6): gas mass resolution for Lagrangian codes (particle mass or typical cell mass); col. (7): ϵ: effective gravitational force resolution (where appropriate this is the gravitational softening length, defined as the effective softening of a Plummer law fit to the actual gravitational force); col. (8): minimum time step; col. (9): average time step; col. (10): number of gas resolution elements within the cluster (number of cells or number of SPH gas particles); col. (11): image smoothing; col. (12): computer used; col. (13): CPU processor hours; col. (14): memory required; col. (15): date of simulation.

REFERENCES FOR CODE DESCRIPTIONS.—(1) Bryan & Norman 1999; (2) Ryu et al. 1993; (3) Couchman et al. 1995; (4) Evrard 1988; (5) Gnedin 1995; (6) Pearce & Couchman 1997; (7) Navarro & White 1993; (8) Owen et al. 1998; (9) Pen 1998; (10) Steinmetz 1996; (11) Wadsley & Bond 1997; (12) Warren & Salmon 1995; (13) Klypin et al. 1992.

The supplied initial displacement field was degraded to the resolution used, 64^3 dark matter particles, simply by sampling every fourth position in each dimension. This rather crude method of resampling, although simple, has the disadvantage of introducing noise into the perturbed particle distribution above the effective Nyquist frequency of the 64^3 particles. Dark matter particles were displaced from a uniformly spaced grid and gas particles were placed on top of the dark matter particles. Particle displacements were scaled to correspond to a start redshift of 49. The center of the final cluster was identified with the density peak within r_{200}.

3.1.2. *Jenkins & Pearce: Parallel Hydra*

This simulation used a parallel version of Hydra, the code just described in § 3.1.1, whose distinguishing feature is its ability to place high-resolution meshes recursively around clustered regions. The SPH calculation used an M4 spline kernel containing an average of 32 particles. Details of the serial version of this code may be found in Couchman et al. (1995), while details of the parallel implementation may be found in Pearce & Couchman (1997).

The simulation was carried out on a Cray-T3D. Initial conditions were laid down by perturbing 128^3 particles distributed in a "glass" configuration. This was generated in the manner described by White (1996), i.e., by evolving a Poissonian distribution of points, with the sign of gravity reversed, over many thousands of expansion factors. To optimize the resolution in the region of interest, the computational volume was divided into two parts, a high-resolution spherical region containing $\frac{1}{4}$ of the volume and centered on the location of the constrained peak, and a coarsely sampled exterior region. Dark matter and gas particles (initially coincident) were placed in the high-resolution region, and dark matter particles only in the exterior region. The coarse sampling was achieved by smoothing the distribution with a nearest grid point (NGP) assignment on a 64^3 mesh, so that, on average, each particle was 8 times more massive than particles in the high-resolution region. This procedure reduced the particle number from 2,097,152 dark matter particles to 1,247,217 of both species, about 1,000,000 of which lay in the high-resolution region. The initial particle positions were set up at $z = 20$ using a trilinear interpolation of the displacement field in the eight mesh points surrounding each particle. Velocities were assigned from the Zeldovich approximation. The center of the final cluster was defined to be the position of the particle with the lowest gravitational potential.

Since this and Couchman's simulation were carried out with the same code, one in parallel and the other in serial mode, any differences in the results must be due to differences in the initial conditions or the choice of integration parameters. We have checked that running Couchman's initial conditions in parallel mode does not alter his results in any significant way.

3.1.3. *Evrard: P^3M-SPH*

The P^3M-SPH code combines the P^3M code of Efstathiou & Eastwood (1981) with an adaptive kernel SPH scheme, as described in Evrard (1988). The simulation for this study employed a two-level mass hierarchy, with a high-resolution (64^3 effective) inner zone of both dark matter and gas surrounded by dark matter at low

resolution (32^3). The N^3 mesh data were generated by NGP subsampling of the original 256^3 displacement field. The mapping of the high-resolution zone was determined by a low-resolution (32^3) N-body simulation; particles within a final density contrast of 6 centered on the group in this run define a Lagrangian mask used to generate the two-level initial conditions of the full run. Masked locations in the 32^3 subsampled field were locally "exploded" to a factor 2 higher linear resolution, generating an effective 64^3 resolution within the nonlinear parts of the cluster. This procedure assures no contamination of low-resolution particles within the cluster in the production run. The run used 30,456 particles for each high-resolution component (gas and dark matter) and 28,961 particles at low resolution, with a 128^3 Fourier mesh for the long-range gravity. The center of the final cluster was defined by the most bound dark matter particle.

The number of interacting neighbors within the smoothing kernel controls the hydrodynamics resolution of the calculation. This parameter was set so that approximately 168 particles lie within a sphere of radius $2h$ around any particle. As discussed by Owen and Villumsen below, the value of this parameter varies considerably among experiments in the literature. The value employed here is larger than "typical" values and reflects a desire to minimize the Poisson noise inherent in the kernel summations required for calculation of the density and pressure gradient terms.

The computation was performed on a local Hewlett-Packard workstation. The modest memory and CPU requirements of this calculation reflect its nature as closer to "everyday" than "state of the art." It is representative of the type of runs used in ensembles to investigate statistical aspects of the cluster population (e.g., Mohr & Evrard 1997).

3.1.4. *Navarro: Grape + SPH*

The code used was the N-body/SPH code described by Navarro & White (1993), adapted to compute gravitational accelerations using a GRAPE-3 board. The neighbor lists needed for the SPH computations are also retrieved from the GRAPE and processed in the front-end workstation. The implementation of these modifications is straightforward and very similar to that described by Steinmetz (1996), where the reader may find far more details.

The initial conditions were realized by perturbing a cubic grid of particles with the displacement field made available with the initial conditions package. The system was divided in two zones, an inner cube of size 38 Mpc that was filled with 40^3 dark matter and 40^3 gas particles, surrounded by a sphere of diameter 64 Mpc. The region outside the inner cube was filled with $\sim 5,000$ low-resolution dark matter particles of radially increasing mass. Initially, gas and dark matter particles were placed on top of each other and were given the same velocities, computed using the Zeldovich approximation. The final cluster center was calculated using a concentric sphere method that isolates the highest density peak iteratively by computing the center of mass of a sphere and successively removing the outermost particle, until only about 100 particles are left.

The simulation was run on the SPARC10/GRAPE-3 system at Edinburgh University.

3.1.5. *Steinmetz: GrapeSPH*

This simulation was performed using GrapeSPH (Steinmetz 1996), a direct summation hybrid N-body/SPH

code especially designed to take advantage of the hardware N-body integrator GRAPE (Sugimoto et al. 1990). It is highly adaptive in space and time through the use of individual particle time steps and individual smoothing lengths. Details of the code such as the adaptive smoothing length or the multiple time-stepping procedure, are presented in Steinmetz & Müller (1993) and in Steinmetz (1996).

The simulation used a multimass technique similar to that described by Porter (1985). First, a low-resolution (32^3 particles) P^{3}M simulation of the full periodic volume was performed. The initial conditions were drawn from the distribution supplied by averaging positions and velocities in cubes of 8^3 particles. At $z = 0$ the cluster that formed near the center was identified and its virial radius, r_{200}, determined. Particles within r_{200} were marked and traced back to redshift $z = 20$. A sphere was then drawn containing all these particles—the high-resolution region. Particles within that sphere were replaced by the corresponding particles drawn from higher resolution initial conditions. Thus, the particle number in the high-resolution region was increased by factors of 8–64. Particles outside the high-resolution region were combined into larger mass nodes using the tree-pruning technique described in Porter (1985). The mass of a particle thus increases logarithmically with distance from the central sphere. Starting from these initial conditions, the full simulation was performed, with gasdynamics followed only in the high-resolution region. The center of the final cluster was defined as the center of mass of the smallest (radius 125 kpc) of a series of seven concentric spheres of progressively decreasing radius. (This agreed to within about 5% with the minimum of the gravitational potential.)

In the hardware integrator GRAPE, the interparticle force is hardwired to obey a Plummer force law. Thus, periodic boundary conditions cannot easily be realized (for a more recent development, see Huss, Jain, & Steinmetz 1999). Because of the tree-pruning, however, the CPU time scales only logarithmically with box size for a given numerical resolution. A typical application thus starts from a very large simulation sphere assuming vacuum boundaries. Since the computational box supplied for this cluster simulation was relatively small, effects due to the finite box size cannot be excluded, and this may also affect the comparison with grid based methods. In order to minimize the effects of finite box size and vacuum boundary conditions, the simulation strategy was slightly modified. Tree pruning was not applied to the original box but to an enlarged box including the 26 neighboring periodic replicas of the original. Hence, vacuum boundaries apply to a surface of radius $r = 1.5 l_{box}$, rather than $r = 0.5 l_{box}$.

A variety of simulations with differing numerical resolution, particle numbers, and size of the high-resolution region were performed. Results from one simulation only have been included in this paper. This probably reflects the best compromise between resolution and computational cost. In this simulation, which took about 28 hr of CPU and 22 Mbyte of memory, $\sim 15,000$ gas and dark matter particles ended up within the virial radius of the cluster at redshift $z = 0$, a resolution similar to that achieved by Evrard, Navarro, Couchman, and Wadsley. The largest simulation carried out had the same number of gas particles but 8 times as many dark matter particles. This run consumed a total CPU time of 254 hr and required 45 Mbyte of memory.

3.1.6. *Wadsley & Bond: P^{3}MG-SPH*

The Wadsley & Bond (1997) P^{3}MG-SPH code used in this cluster comparison combines SPH for the hydrodynamics with an iterative multigrid scheme to solve for the nonperiodic gravitational potential with a particle-particle correction for subgrid forces. A recursive linked list is used to locate neighbor particles for SPH. At each time step, a multipole expansion is used to obtain the gravitational potential boundary conditions on a 128^3 grid. The multigrid technique is quite competitive with fast Fourier transform methods in speed and can more efficiently treat nonperiodic configurations, for which the P^{3}MG-SPH code is designed. It is typically used to compute highly active inner regions at high resolution, with large-scale tides treated using a sequence of progressively lower resolution spherical shells in the initial conditions. The force is augmented by a measured external tidal field evolved using linear theory.

This cluster had a Gaussian filter scale for the peak that was too large for the periodic box size to treat the tidal environment adequately (i.e., the cluster was apodized). To a spherical high-resolution region of radius 25 Mpc, we could add only a single lower resolution shell extending to 32 Mpc in radius. The 25 Mpc choice was based on the region the peak-patch theory (Bond & Myers 1996) suggests would have collapsed. The low-resolution particles had 8 times the mass of the high-resolution ones. The self consistent linearly evolved external shear was also applied to the entire region. There were 74,127 gas and 74,127 dark particles used in the simulation. The initial 256^3 displacement field was sampled at every fourth lattice site to transfer onto the computational grid for the high-resolution region. A similar transfer was done for the low-resolution region, with slight smoothing added. Couchman used the same one-in-four transfer method, probably accounting for the similarities with the Wadsley & Bond result, especially with regard to timing. Discrepancies may be due, at least in part, to his use of periodic boundary conditions. The center of the final cluster was taken to be the center of mass of the largest group in the simulation identified with a standard friends-of-friends group finder.

The computation was run on a DEC Alpha EV5 and required 119 CPU hr and 100 Mbyte of memory. The current version of this code has a significantly accelerated particle-particle section, using tree techniques (the PP section of the old gravity solver slowed by a factor of 10 by $z = 0$). The same computation now takes 33.6 CPU hr and 50 Mbyte of memory.

3.1.7. *Owen & Villumsen: Adaptive SPH*

This simulation was performed with a variant of the SPH method called adaptive smoothed particle hydrodynamics, or ASPH. ASPH generalizes the isotropic sampling of SPH by associating an individual, ellipsoidal interpolation kernel with each ASPH node, the size, shape, and orientation of which is evolved using the local deformation tensor $\partial v_i / \partial x_j$. The goal of the algorithm is to maintain a constant number of particles per smoothing length in all directions at all times for each ASPH particle. This anisotropic sampling allows the ASPH resolution scale to better adapt to the local flow of material as compared with the isotropic sampling of traditional SPH, thereby maximizing the resulting spatial resolution for a given number of particles. Another

way of stating this is to say that, in the frame defined by the kernel, the distribution is locally isotropic.

The ASPH formalism is meaningful only when particles are treated not as particles but as moving centers of interpolation. The effects of momentum nonconservation are minimized so long as internal consistency in the ASPH kernel field is maintained, a condition we enforce by renormalizing the ASPH kernels periodically. The prescription for this renormalization, the ASPH algorithm, and the code used here are described in detail in Owen et al. (1998), and an earlier discussion of ASPH may be found in Shapiro et al. (1996).

The ASPH interpolation between nodes is performed using the bicubic spline interpolation kernel, which formally extends for two smoothing scales, h. Beyond this point, the bicubic spline falls to zero, and therefore only nodes within $2h$ can interact with each other. The local smoothing scales were initialized such that there are roughly two nodes per smoothing scale, so each node "sees" a radius of four nodes, or a total of $(4/3)\pi 4^3 \approx 268$ nodes. Of course, since the bicubic spline weighting falls to zero near the edge of this sampling volume, each node effectively interacts with only about $(4/3)\pi 3^3 \approx 113$ neighbors. While this represents a much larger number of neighboring particles than most contemporary SPH implementations (a more typical value is 1 particle per h, yielding 32 particles in a volume of radius $2h$), it appears that keeping 1.5–2 particles per h yields more reliable results for a wide variety of hydrodynamical test problems (see also Balsara 1995). Evrard's SPH simulation also used a large number of interacting particles. The disadvantage of this choice, of course, is that it decreases the effective resolution. An additional feature of the code is that it uses a compact, higher order interpolation kernel for the artificial viscous interactions in an effort to more closely confine the effects of the artificial viscosity to shocked regions. The gravitational interactions are evaluated using a straight, single-level particle-mesh (PM) technique.

This experiment was performed using 32^3 dark matter and 32^3 ASPH particles, and a 256^3 PM grid for the gravity. Since there are equal numbers of ASPH and dark matter particles, each dark matter particle is 9 times as massive as an ASPH particle. The initial conditions were generated for $z = 20$ by perturbing the 2×32^3 ASPH and dark matter particles (initially exactly overlaying each other) from a cubical lattice with trilinear interpolation based upon the supplied displacement field, and assigning velocities using the Zeldovich approximation. The center of the final cluster was defined through an iterative approach, similar to that used by Steinmetz. In this case, the radius of each successive sphere was shrunk by a factor of 0.9 and the iterations were stopped when the center of mass shifted by less than a small tolerance.

It is worth commenting on the fact that with only 32^3 ASPH and dark matter particles, this is by far the lowest resolution of the SPH experiments presented in this paper. This is primarily due to the fact that at the time this experiment was performed our three-dimensional ASPH code had only just been completed, and this was one of the first problems tackled with that (then) highly experimental code. Because of the lateness of our entry into this project, we only had time to confirm that the experiment appeared to have run successfully and submit that initial run. The current version of our three-dimensional ASPH code is

competitive with other contemporary cosmological hydrodynamical codes. Despite these limitations, though, it is interesting to compare the results of this simulation with the others in order to quantify how well the regions that are resolved match the results of the higher resolution models.

3.2. Grid-based Methods
3.2.1. Bryan & Norman: SAMR

A newly developed, structured, adaptive mesh refinement (SAMR) code was used to perform this simulation. This method was designed to provide adaptive resolution while preserving the shock-capturing characteristics of an Eulerian hydrodynamics scheme. The code identifies regions requiring higher resolution and places one or more finer submeshes over these areas in order to better resolve their dynamics. There is two-way communication between a grid and its "child" meshes: boundary conditions go from coarse to fine, while the improved solution on the finer mesh is used to update the coarse "parent" grid. The grid placement and movement is done automatically and dynamically, so interesting features can be followed at high resolution without interruption. Since subgrids can have sub-subgrids, this process is not limited to just two levels. The control algorithm for advancing the grid hierarchy is similar to that suggested by Berger & Colella (1989), and the equations of hydrodynamics are solved on each grid with a version of the piecewise parabolic method (PPM) modified for cosmology (Bryan et al. 1995). Dark matter was modeled with particles, and gravitational forces were computed via an adaptive particle-mesh scheme. Poisson's equation was solved on each mesh using the fast fourier transform.

The simulation was initialized at $z = 30$ with two grids already in place. The first is the root grid covering the entire 64 Mpc^3 domain with 64^3 cells. The second grid is also 64^3 cells but is only 32 Mpc on a side and is centered on the cluster, yielding an initial cell size of 500 kpc (the initial conditions were provided at higher resolution but were smoothed with a sharp k-space filter where appropriate). The refinement criteria was based on local density, so any cell with a baryon mass of 3.5×10^9 $M_\odot$ or more was refined, but only within the central, high-resolution region. At $z = 0.5$, the hierarchy consisted of more than 300 grids spread out over seven levels of refinement. Each level had twice the resolution of the one above, producing, in very small regions, a cell size of 8 comoving kiloparsecs. The final cluster center adopted was the cell-center of the cell with the highest baryonic density. The simulation was carried out on four processors of an SGI Power Challenge at the National Center for Supercomputing Applications (NCSA).

3.2.2. Cen, Bode, Xu & Ostriker: TVD

This simulation employed a new shock-capturing Eulerian cosmological hydrodynamics code based on Harten's total variation diminishing (TVD) scheme (Harten 1983) and described in Ryu et al. (1993). The original TVD scheme was improved by adding one additional variable (entropy) and its evolution equation to the conventional hydrodynamics equations. This improvement eliminates otherwise large artificial entropy generation in regions where the gas is not shocked. Details of this treatment can be found in Ryu et al. (1993). The code is able to capture a strong shock within 1–2 cells and a sharp density discontin-

uity within 3–5 cells. Poisson's equation is solved using the fast Fourier transform. The code is accurate in terms of global energy conservation to about 1%, as gauged by the Layzer-Irvine equation.

Initial conditions were laid down on a 512^3 uniform grid, using the particle positions, velocities, and gas densities provided. The initial gas temperature was set to a low value, 113 K. The total number of particles was 256^3, and the total number of fluid cells was 512^3. The simulation started at $z = 40$. The final cluster center was taken to be the cell with the highest X-ray luminosity.

The simulation was run on an IBM SP2 at the Cornell Theory Center. Sixty-four SP2 processors were used for the simulation for about 83 wall-clock hr with 600 time steps. The code is well parallelized on the SP2 (as well as on the Cray-T3E) and achieves an efficiency of about 50% on 64 SP2 processors (Bode, Xu, & Cen 1996).

3.2.3. Pen: Moving Mesh Hydrodynamics

The simulations were all performed with an early version of the moving mesh hydrodynamics and N-body code (MMH; Pen 1995, 1998). Its main features are a full curvilinear TVD hydro code with a curvilinear PM N-body code on a moving coordinate system. The full Euler equations are solved using characteristics in explicit flux-conservative form. The curvilinear coordinates used in the code are derivable from a gradient of the Cartesian coordinate system. If x^i are the Cartesian coordinates, the curvilinear coordinates are $\xi^i = x^i + \partial^i_\xi \phi(\xi)$. The transformation is completely specified by the single potential field $\phi(\xi, t)$. During the evolution any one constraint can be satisfied by the grid. In our case, we follow the mass field such that the mass per unit grid cell remains approximately constant. This gives all the dynamic range advantages of SPH combined with the speed and high resolution of grid algorithms. For reasons of CPU economy (the computational cost increases linearly with compression factor), this run was constrained to compress by at most a factor of 10 in length, or a factor of 1000 in density.

The potential deformation maintains a very regular grid structure in high-density regions. The gravity and grid deformation equations are solved using a hierarchical multigrid algorithm for linear elliptic equations. These are solved in linear time and are asymptotically faster than the fast Fourier transform gravity solver. At the same time, adaptive dynamic resolution is achieved. The gravitational softening of 45 kpc listed in Table 1 applies to the central region of the cluster; the average softening is 450 kpc. The final cluster center was identified with the minimum in the gravitational potential.

The algorithmic cost per particle per time step is very small, ~ 300 FLOP (floating point operations). The cost for the grid deformation, gravity, and hydrodynamics adds about 20 kFLOP per grid cell per time step. If memory is available, we always use 8 particles per grid cell, at which point the particles account for only a small portion of the computation time. This ensures that we are unlikely to encounter artifacts due to two-body relaxation.

The code runs in parallel on shared memory machines without load-balancing problems. The simulation was carried out using a 128^3 grid and 256^3 particles. Currently each time step takes 60 s on a 16 processor Origin 2000 at 195 Mhz. The whole run takes 1600 time steps, or about 1 day. At the time the actual simulations were performed, the best available machine was a 75 Mhz R8k Power Challenge, where the run on 8 processors took 60 hr.

Initial conditions were specified on an initially uniform grid. The fluid perturbation variables were set up on the grid, and particles were displaced using the Zeldovich approximation. (At the time of writing, the code no longer uses the Zeldovich approximation but instead varies the mass of each particle.) The initial grid can now be adjusted to resolve hierarchically any region of interest with arbitrary accuracy. We expect the new version to perform significantly better.

3.2.4. Gnedin: Smooth Lagrangian Hydrodynamics

In this code, the hydrodynamical evolution of the gas is followed using the smooth Lagrangian hydrodynamics or SLH method (Gnedin 1995), in which all physical quantities are defined in quasi-Lagrangian space, q^k, and Eulerian positions, x^i, are considered dynamical variables. The imaginary mesh connecting Eulerian positions, x^i, thus moves with the fluid until one of eigenvalues of the deformation tensor, $A^i_k \equiv \partial x^i / \partial q^k$, becomes smaller than the predefined softening parameter, λ_*. Then in the direction corresponding to this eigenvalue the mesh gradually decelerates and progressively approaches (but never fully reaches) the locally stationary mesh, until (and if) the corresponding eigenvalue of the deformation tensor begins to increase. This process of softening of the Lagrangian flow prevents severe mesh distortions that can cause the stability and accuracy of a purely Lagrangian code to deteriorate. The gravitational force in the code is computed using the P^3M method and is subject to the gravitational consistency condition as described in Gnedin & Bertschinger (1996).

Initial conditions were set up by sampling the supplied fields on a 64^3 mesh and using the Zeldovich approximation to advance the dynamic variables to $z = 20$. The cluster center was defined using the DENMAX algorithm.

3.2.5. Yepes, Khokhlov, & Klypin: PM-FCT

The code used for this simulation is a combination of an Eulerian hydrodynamical code based on the flux-corrected-transport (FCT) technique (Boris & Book 1973, 1976) and a standard particle-mesh N-body code (Kates, Kotok, & Klypin 1990). It uses the low phase error algorithm, whereby phase errors in convection are reduced on the uniform grid to fourth order (Boris & Book 1976; Oran & Boris 1986). This algorithm is applied to the hydrodynamics equations in one dimension. At each time step these are first integrated by FCT for a half-step to evaluate time-centered fluxes; the FCT is then applied to a full time step.

Multiple dimensions are treated through directional time step splitting. In multiple dimensions, the code has overall second-order accuracy in regions where the flow is continuous and provides a sharp, nonoscillating solution near flow discontinuities. To avoid excessive temperature fluctuations at shocks, the gas density is smoothed over the seven nearest nodes (one cell in each direction) when estimating the temperature from the total energy, velocity, and density. This smoothing is done only for temperature estimates. Tests of the code and applications to cosmological problems may be found in Klypin, Kates, & Khokhlov (1992) and Yepes et al. (1995, 1996).

The code has been fully parallelized for various shared memory platforms. The simulation reported here was performed on the CRAY-YMP at CIEMAT (Spain) using four
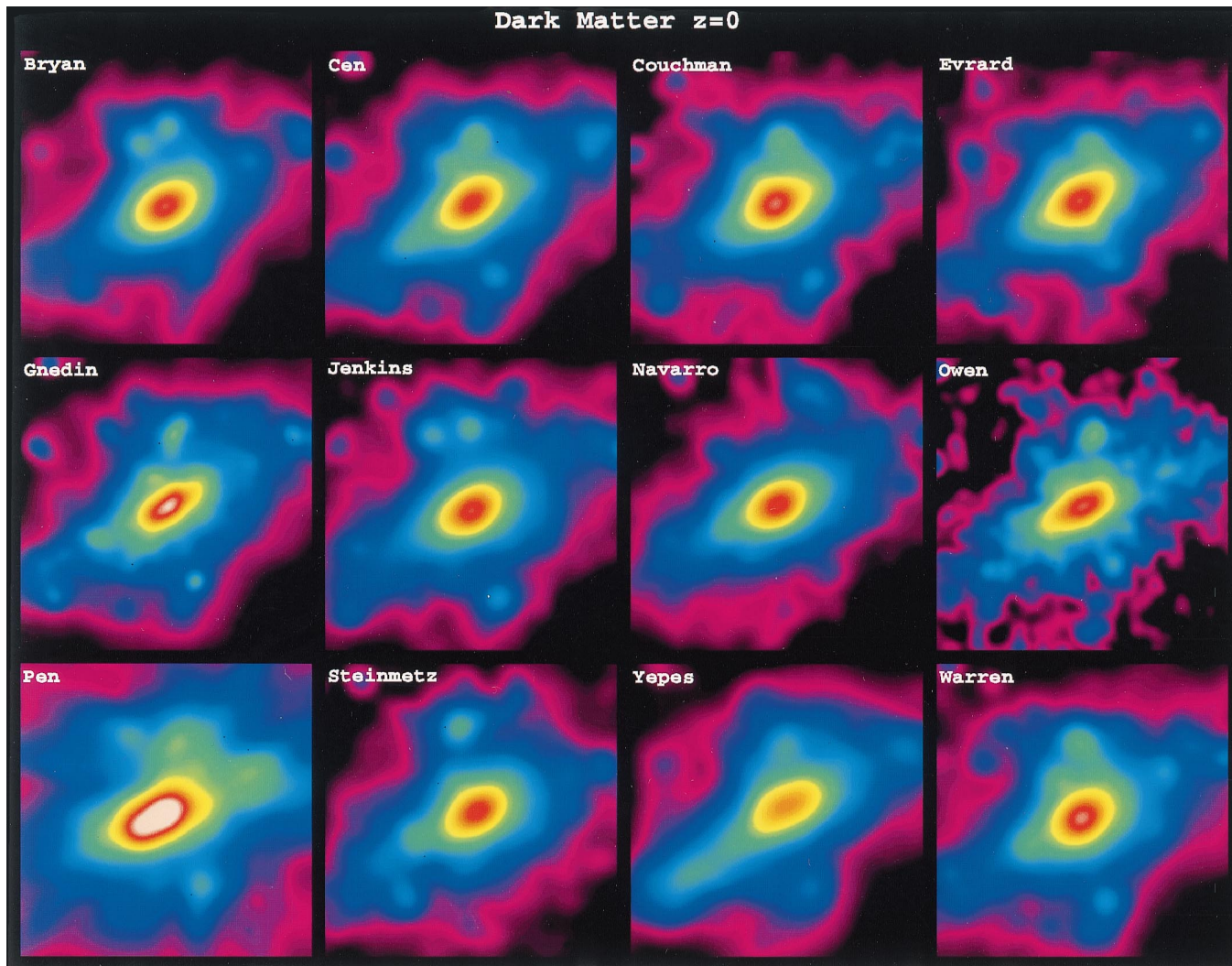
Fig. 1.—Projected dark matter density at $z = 0$. The images, covering the inner 8 Mpc of each simulation cube, have been smoothed using the standard Gaussian filter of 250 kpc half-width described in the text. Wadsley's simulation, not shown here or in Fig. 2, has a similar appearance to Couchman's.

processors simultaneously. Because of memory limitations, the supplied initial conditions were resampled from the original 256^3 grid onto a coarser grid with 160 cells and particles per dimension. The initial particle positions were set up at $z = 20$ using cloud-in-cell interpolation of the original displacement field and velocities were assigned by means of the Zeldovich approximation. The cluster center was found iteratively from the center of mass of the particle distribution in spheres of radius equal to 2 cells.

3.3. Dark Matter Only—Warren Tree

This dark matter only simulation was carried out using a parallel tree code (Warren & Salmon 1993, 1995) on 128 processors of the 512 processor Intel Delta at Caltech. The algorithm computes the forces on an arbitrary distribution of masses in a time that scales with the particle number, N, as $N \log N$. The accuracy of the force calculation is analytically bounded and can be adjusted via a user defined parameter.

Initial conditions were obtained by perturbing the masses of the particles in proportion to the values of the supplied initial density field, starting at a redshift of 63. Growing

mode velocities were assigned using the Zeldovich approximation. The initial conditions were coarsened at radii exceeding 24 Mpc by grouping cells 8:1, resulting in a total of 5,340,952 dark-matter particles in the simulation. Periodic boundary conditions were implemented by using the tree code to obtain forces from the 26 neighboring cube images and an analytic treatment for the remainder. The initial portion of the simulation (to $z = 9$) was performed with a comoving Plummer softening of 50 kpc and a logarithmic time step. At $z = 9$, the softening was fixed at 5 kpc in physical coordinates, and a global time step of .005 Gyr was used, resulting in 2550 total time steps for the simulation. The center was defined as the particle with the highest density, smoothed with a spline kernel of width 20 kpc.

The upper limit for the fractional interaction force error was set to 0.005. In the initial stages of the simulation, about 1200 interactions per particle were computed. Near the end, this had grown to about 2300 interactions per particle. In terms of wall-clock time, this corresponded to about 144 s per time step initially, and 215 s per time step toward the end, representing a sustained throughput of roughly 1.5 GFLOP on the 128 processors.
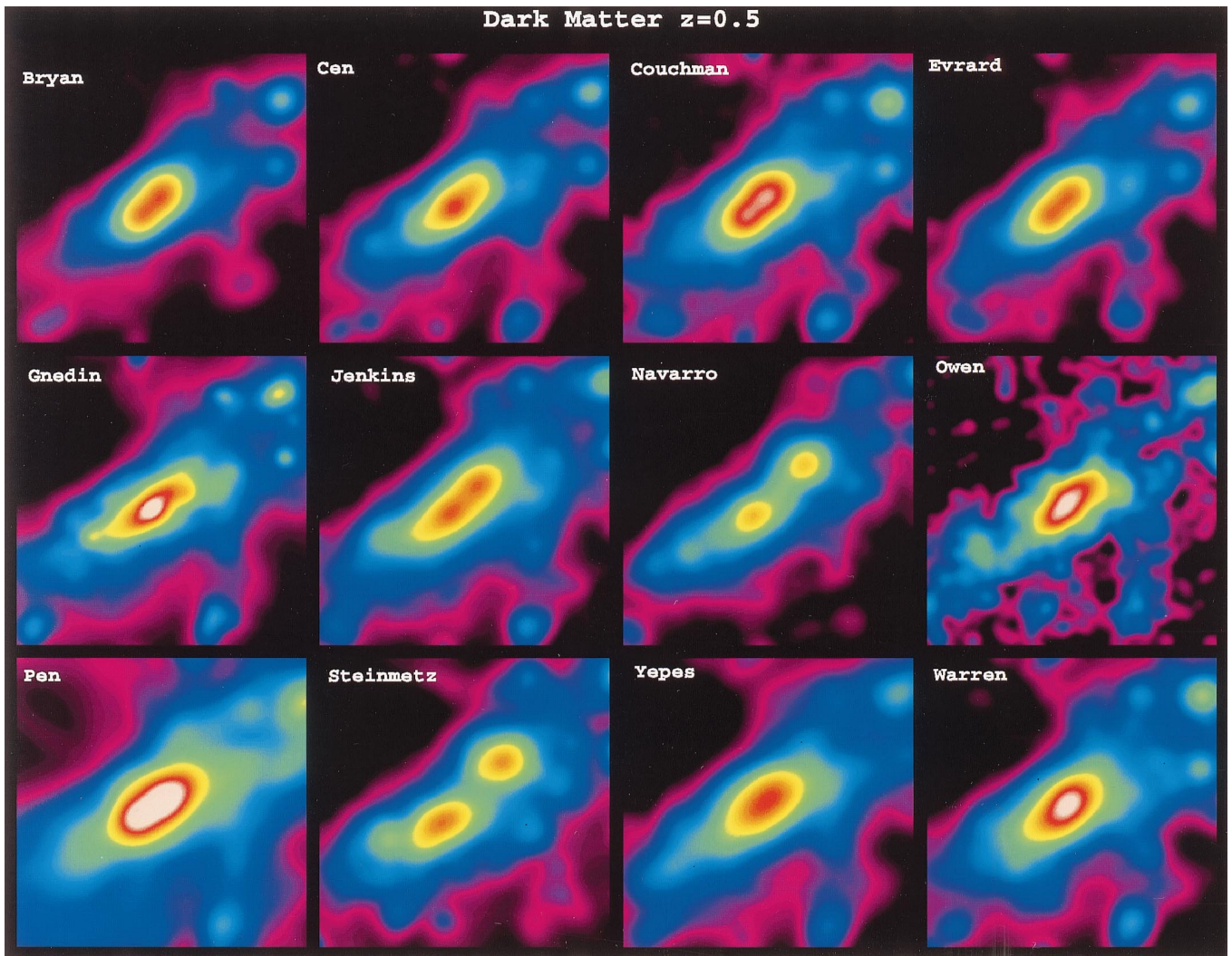
FIG. 2.—Projected dark matter density at $z = 0.5$. The images, covering the inner 8 Mpc of each simulation cube, have been smoothed using the standard Gaussian filter of 250 kpc half-width described in the text.

4. RESULTS

We first present a qualitative comparison of the results of the different simulations using a selection of the images. We then discuss quantitative results for the bulk properties and radial profiles of the clusters.

4.1. Images

The images display projections of the following quantities in the inner 8 Mpc cube of each simulation:

1. the dark matter density at $z = 0$ (Figs. 1 and 8) and $z = 0.5$ (Fig. 2);
2. the gas density at $z = 0$ (Fig. 3) and $z = 0.5$ (Fig. 4);
3. the gas temperature at $z = 0$ (Fig. 5) and $z = 0.5$ (Fig. 6);
4. the X-ray luminosity at $z = 0$ (Fig. 7).

In Figures 1–6, the standard smoothing (250 kpc) was used, whereas in Figures 7 and 8 the optimal smoothing chosen by each simulator was used (see Table 1). The time elapsed between the two epochs shown in the figures is 6×10^9 yr, almost exactly one-half the dynamical time of the final cluster [defined as $t_{\text{dyn}} = 2\pi(r_v^3/GM)^{1/2}$ where r_v is the virial

radius and M the mass within it]. Warren's dark matter simulation is illustrated only in Figures 1, 2, and 8, in the bottom right-hand corner occupied in the remaining figures by Wadsley's simulation, which was the last to be completed. Wadsley's dark matter distribution has a very similar appearance to Couchman's.

4.1.1. Dark Matter Density

All simulations show a pleasing similarity in the overall appearance of the projected dark matter density at the final epoch (Figs. 1 and 8). The size, shape and orientation of the main mass concentration are very similar in all cases. The cluster is elongated in the direction of a large filament—clearly visible at $z = 0.5$ (Fig. 2)—along which sublcumps are accreted onto the cluster. There are, however, noticeable differences at both epochs in the substructures present in the various simulations. These differences are due to discrepancies in the boundary conditions (assumed to be isolated in Navarro, Steinmetz, and Wadsley and periodic in the rest), in the treatment of tidal forces, and in the effective timing within the different simulations.

The models have been evolved for at least 21 expansion factors, and inaccuracies in the initial conditions, tidal
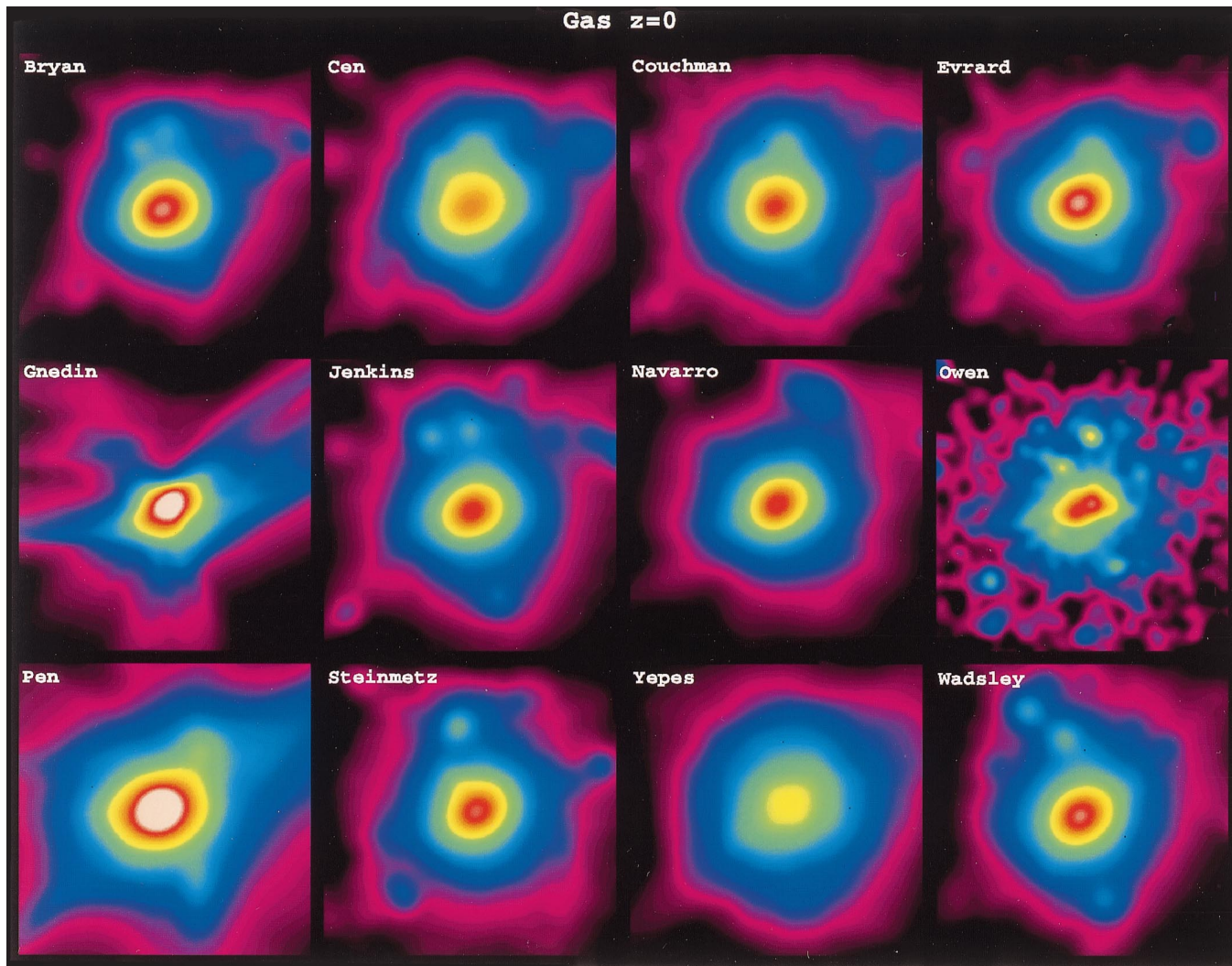
Fig. 3.—Projected gas density at $z = 0$. The images, covering the inner 8 Mpc of each simulation cube, have been smoothed using the standard Gaussian filter of 250 kpc half-width described in the text.

forces, or integration errors in the linear regime lead to a lack of synchrony at later times. These timing discrepancies are manifest in the differing relative positions of some subclumps at $z = 0.5$ and are still apparent at $z = 0$. For example, there are two distinct substructures in Figures 1 and 8 to the northwest of the main clump at $z = 0$ in slightly different positions in Bryan, Cen, Jenkins, Owen, Pen, and Warren. In Couchman, Evrard, Gnedin, Steinmetz, and Yepes, one of these substructures is already merging with the central clump, while in Navarro both of them have merged. The differences in the overall shape and orientation of the main concentration are largely due to a mismatch in the epoch at which substructures are accreted.

With a uniform, 250 kpc, smoothing significant noise is visible in Owen. Figure 8 shows the dark matter distribution at $z = 0$, this time using the smoothing considered as optimal by each simulator to display what they considered to be real structure. There is a larger variety of structure in these high-resolution images than in the uniform smoothing case of Figure 1. The simulations of Jenkins and Warren that have the largest number of resolution elements also have the largest number of satellite structures. Varying numbers of these can be seen in other images, although because of the slight timing differences they often appear in

different locations. The low- and intermediate-resolution simulations of Cen, Gnedin, Owen, and Yepes look quite similar when the standard smoothing or the smoothing of choice is used.

4.1.2. *Gas Density*

At the present epoch, the gas in all simulations (Fig. 3) is rounder than the dark matter—a manifestation of the isotropic gas pressure—and has only a residual elongation along the accretion filament. Most of the secondary clumps seen in the dark matter are also seen in the gas, but they are clearly more diffuse. At $z = 0.5$ (Fig. 4), shortly before the final large merger, the timing differences discussed above are quite apparent. In some cases, the final major merger is already quite advanced, but in others two large subclumps are still clearly visible.

With this smoothing, the sampling in Owen is poor and Yepes' comparatively low resolution is more apparent than in the corresponding dark matter image. In Owen's case, the underlying asphericity of the SPH sampling is lost when a fixed smoothing length is used; less noisy images result when the geometry of the hydrodynamical sampling is maintained, as in the X-ray image in Figure 7 below.
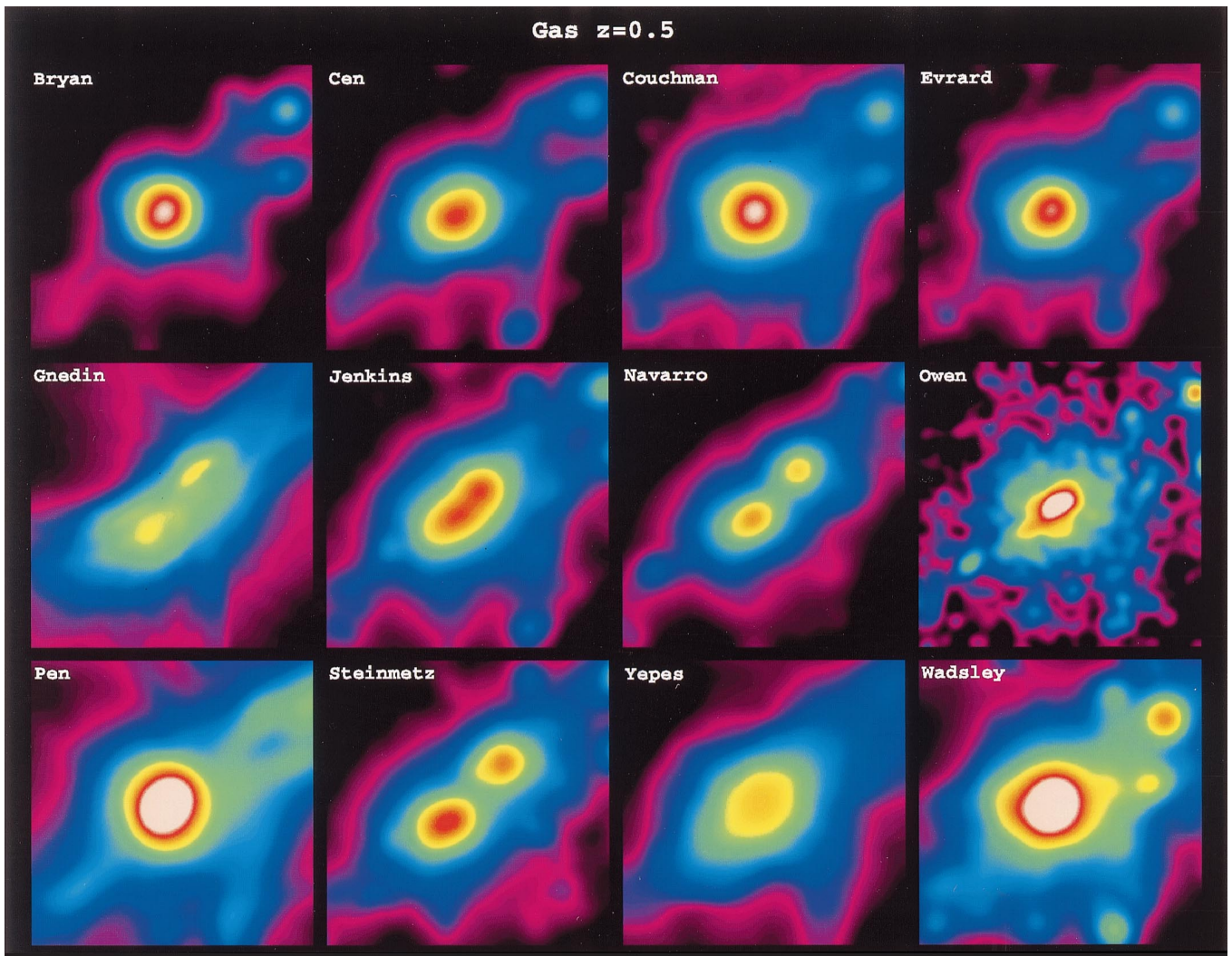
FIG. 4.—Projected gas density at $z = 0.5$. The images, covering the inner 8 Mpc of each simulation cube, have been smoothed using the standard Gaussian filter of 250 kpc half-width described in the text.

4.1.3. *Gas Temperature*

The gas temperature images (Figs. 5 and 6) show the most interesting differences between the simulations. These are particularly striking at $z = 0.5$ when the slight timing differences apparent in the dark matter and gas density plots produce quite dramatic differences in temperature structure. In particular, in the simulations by Jenkins, Navarro, and Steinmetz, in which the final major merger has not yet occurred at $z = 0.5$, an annulus of shock-heated material is evident between the two approaching clumps, surrounding the axis of collision. In Evrard and Owen, the merger is further advanced, but some residue of the annular structure remains. The simulations of Bryan, Cen, Gnedin, and Yepes are yet further advanced, and while their temperature plots show similar departures from symmetry, the annular structure is no longer evident. In Couchman and Wadsley, the merger is nearly complete and the temperature distribution appears close to spherically symmetric.

At $z = 0$ the plots are broadly similar and most of the temperature structure, both inside the cluster and in the outer regions of the clusters, is reproduced similarly in the different simulations.

4.1.4. *X-Ray Surface Brightness*

Like the dark matter distributions in Figure 8, the X-ray surface brightness images in Figure 7 were generated using each simulator's smoothing of choice. Since the X-ray surface brightness is calculated by integrating $\mathscr{L}_X = \rho^2 T^{1/2}$, these images are similar to those of the surface density (Fig. 3), except that higher weight is given to the central parts of the clumps. As a result, the central intensity is strongly dependent on resolution. In the region where the bulk of the X-rays are produced, most images are quite similar. However, there are large differences in the number and brightness of satellite structures. Jenkins and Wadsley produced the largest number of such structures, followed by Bryan and Steinmetz. Again, the substructures appear in different places because of the timing discrepancies discussed above.

The high-resolution grid codes of Bryan and Pen and the intermediate-resolution grid code of Gnedin show sharper structure in the low-density regions than the SPH codes, a reflection of their better treatment of shocks in low-density regions. Bryan's, Pen's, and all but Owen's SPH codes have high central resolution and generally produce brighter
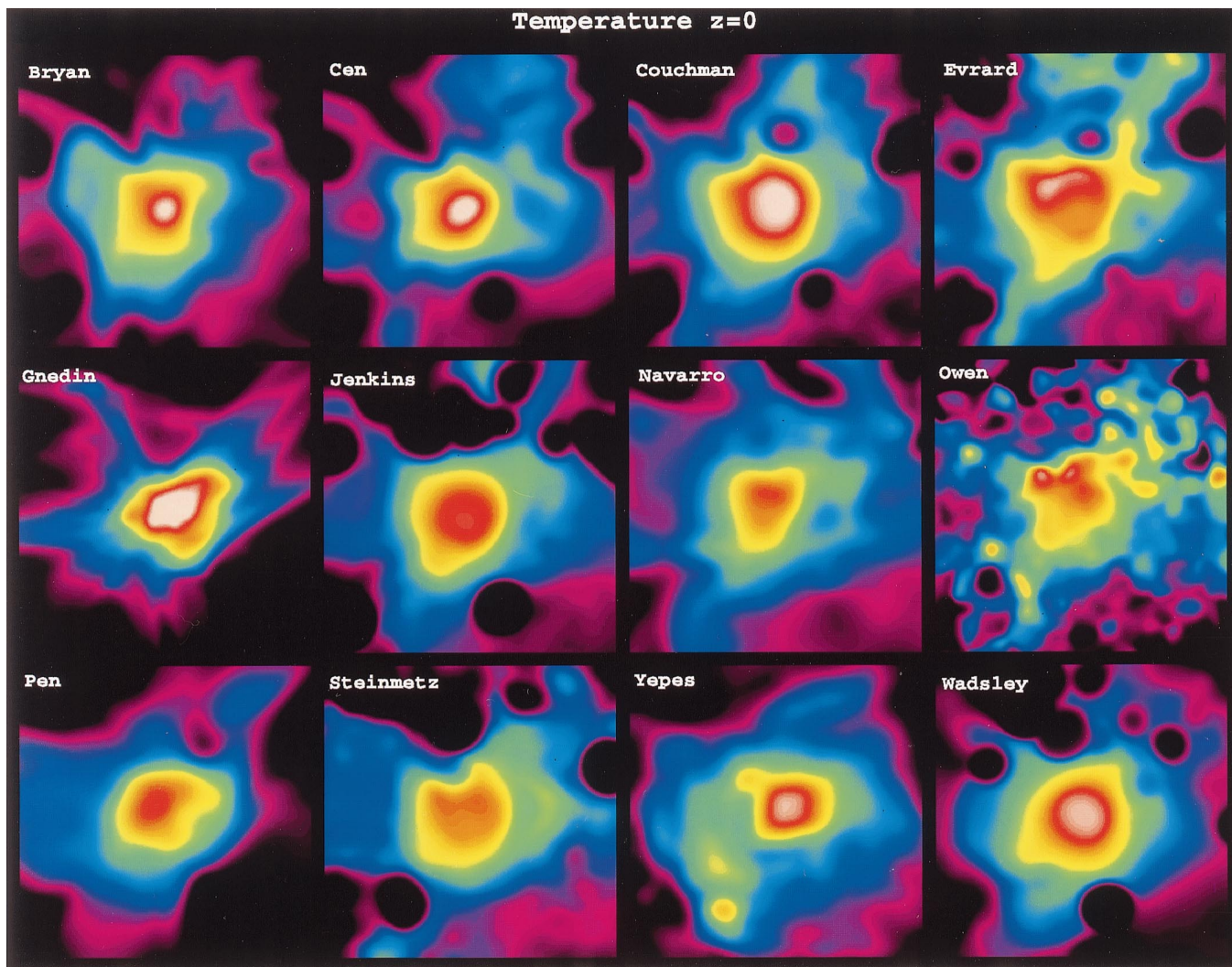
Fig. 5.—Integrated, mass-weighted gas temperature at $z = 0$. The images, covering the inner 8 Mpc of each simulation cube, have been smoothed using the standard Gaussian filter of 250 kpc half-width described in the text. (The roughly circular "cut-out" regions seen in the outer parts of this and Fig. 6 are associated with cool, infalling clumps of size comparable to the resolution of the smoothed image (see Figs. 3 and 4); the edges are enhanced by the choice of color table.)

central regions than the low- and intermediate-resolution grid codes.

4.2. Global Properties

All simulators were requested to calculate global properties of their clusters at the final time. The cluster was defined to be the material lying within a spherical region around the center, of radius such that the mean enclosed mass density is 201 times the critical value. In practice, each simulator was left free to choose a preferred algorithm for locating the cluster center since this choice is part of the uncertainties that we are trying to assess. (The algorithms used in each case are described in § 3.) The mean value of the cluster radius, averaged over all simulations, was $r_{200} = 2.70$ Mpc, with an rms scatter of 0.04. We display the global properties of the clusters in graphical form in Figure 9 and discuss the different quantities one at a time. In each panel in this figure, the simulations are arranged, from left to right, in order of decreasing resolution, which is taken to be the maximum of the spatial resolution for the gas at cluster

center (col. [4] of Table 1) and the gravitational force resolution (col. [7] of Table 1). Open circles are used to represent SPH simulations and filled circles grid-based simulations.

The simplest property of the cluster is its total mass, and all simulations agreed on a value just over 10^{15} $M_\odot$, to within better than 10%. Differences arise from resolution and timing effects. Among the grid-based codes, there is a clear trend of decreasing mass with decreasing resolution. The timing discrepancies discussed in § 4.1 affect the position of substructures and thus the estimates of the cluster mass. For example, among the SPH codes, Jenkins, Navarro, and Steinmetz find slightly smaller masses than the others because of a significant lump clearly visible in Figures 7 and 8 that falls just outside the cluster boundary in their simulations but just inside it in the others. This is a result of the late formation of their clusters, apparent in Figure 2.

The velocity dispersion of the dark matter particles within the cluster is also reproduced to better than 10% in
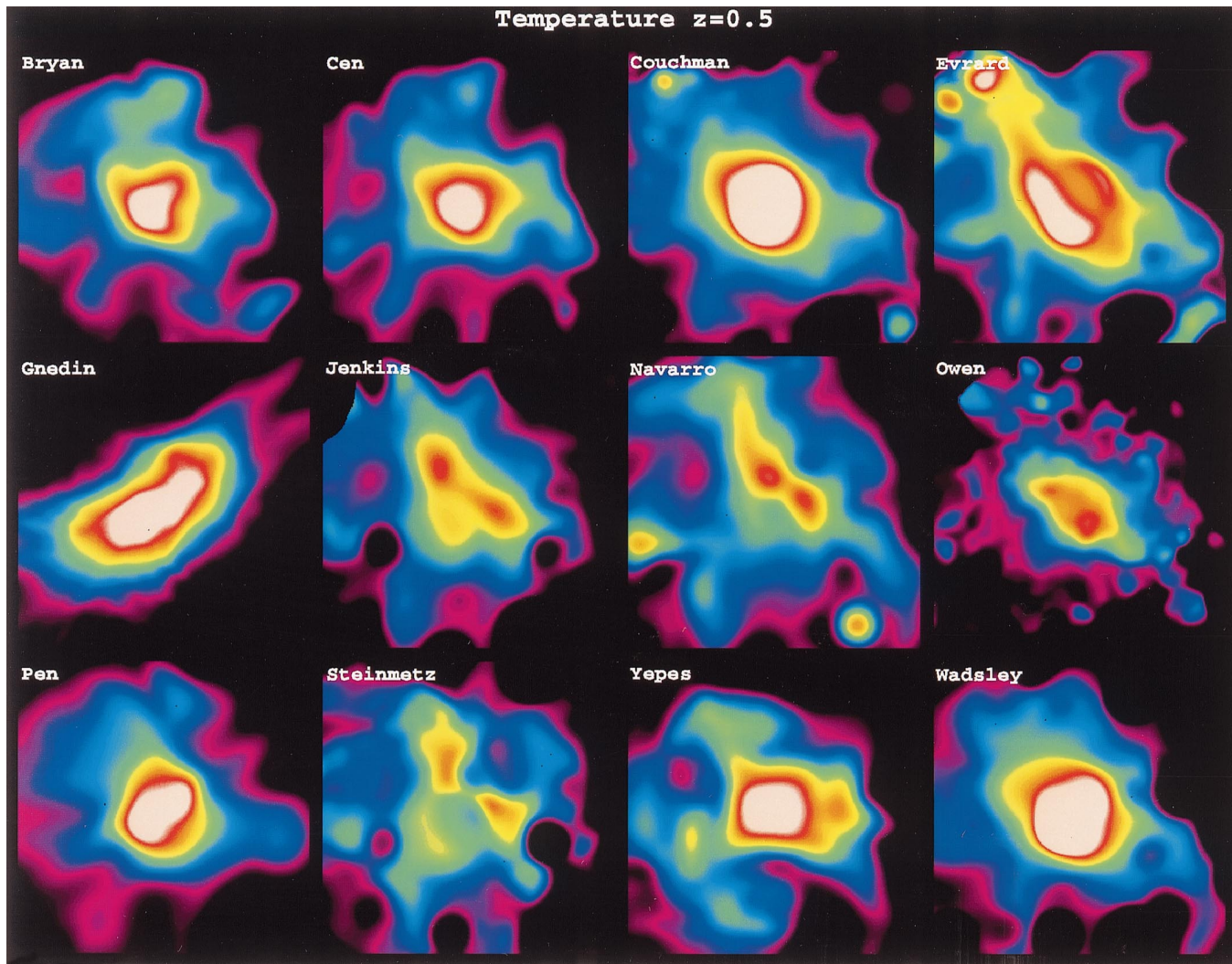
FIG. 6.—Integrated, mass-weighted gas temperature at $z = 0.5$. The images, covering the inner 8 Mpc of each simulation cube, have been smoothed using the standard Gaussian filter of 250 kpc half-width described in the text.

all simulations except that of Yepes, whose low value reflects the low force resolution of his simulation. (The quantity plotted is the one-dimensional velocity dispersion, calculated as $\sigma/\sqrt{3}$, where σ is the full three-dimensional velocity dispersion in the rest frame of the cluster.) There is some tendency for the simulations that produced the largest total masses also to give the largest velocity dispersions, but the correspondence is not exact, reflecting the fact that the cluster is not in virial equilibrium to better than 10% and that the actual virial ratio depends on the detailed positions of infalling clumps.

As might be expected, although still quite good, the agreement on the properties of the gas is noticeably worse. The total amount of gas is most interestingly expressed as a fraction of the total cluster mass. The overall gas fraction in the model universe is 10%, and the highest resolution grid simulations find a cluster gas fraction that is almost exactly equal to this. Lower resolution grid simulations find progressively smaller gas fractions, reflecting differential resolution effects in the treatment of dark matter and gas in these codes. There is excellent overall agreement among the SPH models except for the lowest resolution one: everyone except Owen finds a gas fraction very close to 0.09. There seems to be a systematic offset between the SPH models and

the highest resolution grid models, but there is no clear indication of what may be causing this difference. We explore this issue further in the next section by considering the radial dependence of the gas fraction.

As a measure of temperature, all simulators calculated a mean, mass-weighted temperature for all the gas within the cluster. Everyone found a value between 4.9 and 5.9×10^7 K. Figures 5 and 6 suggest that some of the differences result from the timing differences discussed above which produce slightly different histories for the clusters just prior to $z = 0$. It is encouraging that the rms scatter in the measured mean temperature is less than $\pm 7\%$. An even smaller scatter, $\pm 5\%$, is found for the ratio of specific dark matter kinetic energy to gas thermal energy, $\beta = \mu m_p \sigma_{dm}^2 / 3kT$, if Yepes' low value is excluded. (Here μ denotes the mean molecular weight and m_p the proton mass.) This is further evidence that the differences in velocity dispersion and temperature result from slightly different dynamical histories rather than from differences in the treatment of the gas. Most simulations give $\beta \simeq 1.17$, indicating that nonthermal or bulk turbulent motions contribute to the support of the gas. The ratio of bulk kinetic to thermal energy in the gas, plotted in the next panel of Figure 9, is indeed about 15%. This ratio correlates well with β, but with small residuals
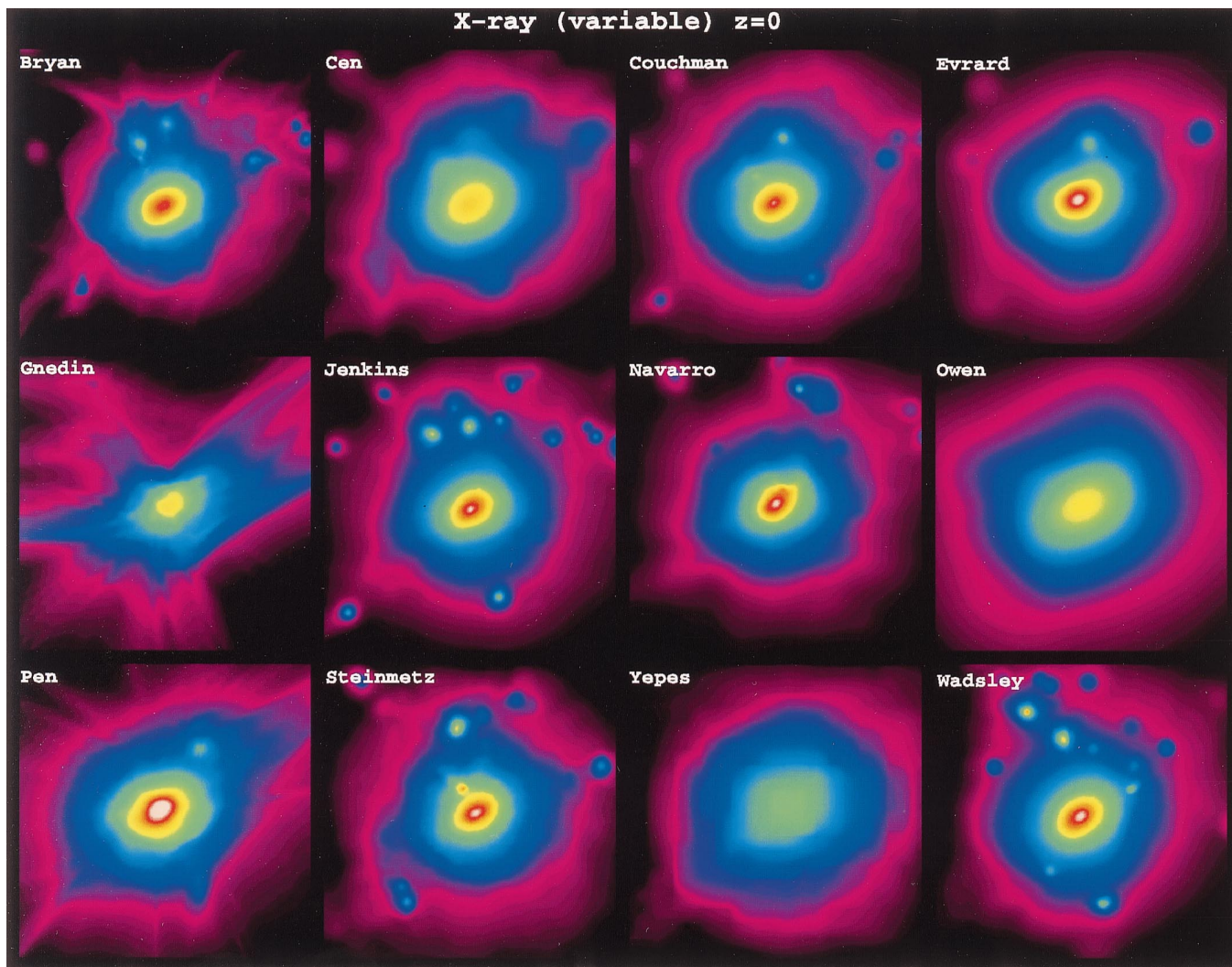
Fig. 7.—Projected X-ray luminosity at $z = 0$. The images, covering the inner 8 Mpc of each simulation cube, have been smoothed with the filter chosen by each author to best portray the results of each simulation (see Table 1).

that reflect slight departures from virial equilibrium. The agreement on the values of β and U_{kin}/U_{therm} indicates that the shock-capturing properties and the efficiency with which infall kinetic energy is thermalized in shocks are similar in the SPH and grid-based codes, at least in the regime explored in this simulation. Most simulators obtained values of about 3.6×10^{62} ergs for the bulk kinetic energy, except Gnedin and Wadsley, who found values about 25% smaller. Lower turbulent energies probably result from some combination of smaller noise-induced motion, greater viscous damping, and, in Wadsley's case, a more dynamically advanced state, but the actual factors responsible in each case are unclear.

There is substantially less consensus about the estimated X-ray luminosities of the cluster, calculated approximately as $\int \rho^2 T^{0.5} \, dV$, and so given in units of $M_\odot^2 \; K^{1/2} \; Mpc^{-3}$. The values found span a range of a factor of ~ 10, or a factor of ~ 5 if we exclude Yepes' low-resolution model. Resolution effects also account for the small values obtained by Cen and Owen. The largest values were obtained in the intermediate- and high-resolution grid-based simulations of Gnedin and Pen, respectively, and in Evrard's SPH simulation. Evrard's and Wadsley's models produced larger X-ray luminosities than other SPH simula-

tions because their clusters are in a slightly more advanced (and more active) dynamical state. The higher luminosities from the high-resolution grid-based codes are due to their slightly more concentrated central gas distributions (see Fig. 3 and § 4.3 below). Because the total X-ray luminosity is sensitive to the structure of the inner few hundred kiloparsecs of the cluster, it fluctuates quite strongly in time and is very sensitive to simulation technique.

As a final test, we compare the shapes of the clusters, as measured by the inertia tensors, $\mathscr{I} = \sum m_i x_i x_j / \sum m_i$, for both the dark matter and the gas within the spherical region that defines the cluster. We label the eigenvalues of this tensor $a^2 > b^2 > c^2$ and define the axial ratios to be a/b and a/c. As can be seen in Figures 1 and 3, the cluster is aspherical, with the orientation of its longest axis reflecting its formation by infall along a filament. The axial ratios shown in Figure 9 show, in fact, that the cluster is triaxial. The dark matter distribution (circles in Fig. 9) is considerably more aspherical than the gas (crosses) in all cases except Gnedin's. There is generally good agreement amongst the different simulations, although there are a few anomalies. For example, Owen finds the smallest axial ratios for the dark matter distribution even though the inner regions of his cluster appear quite elongated in Figure 1. This is prob-
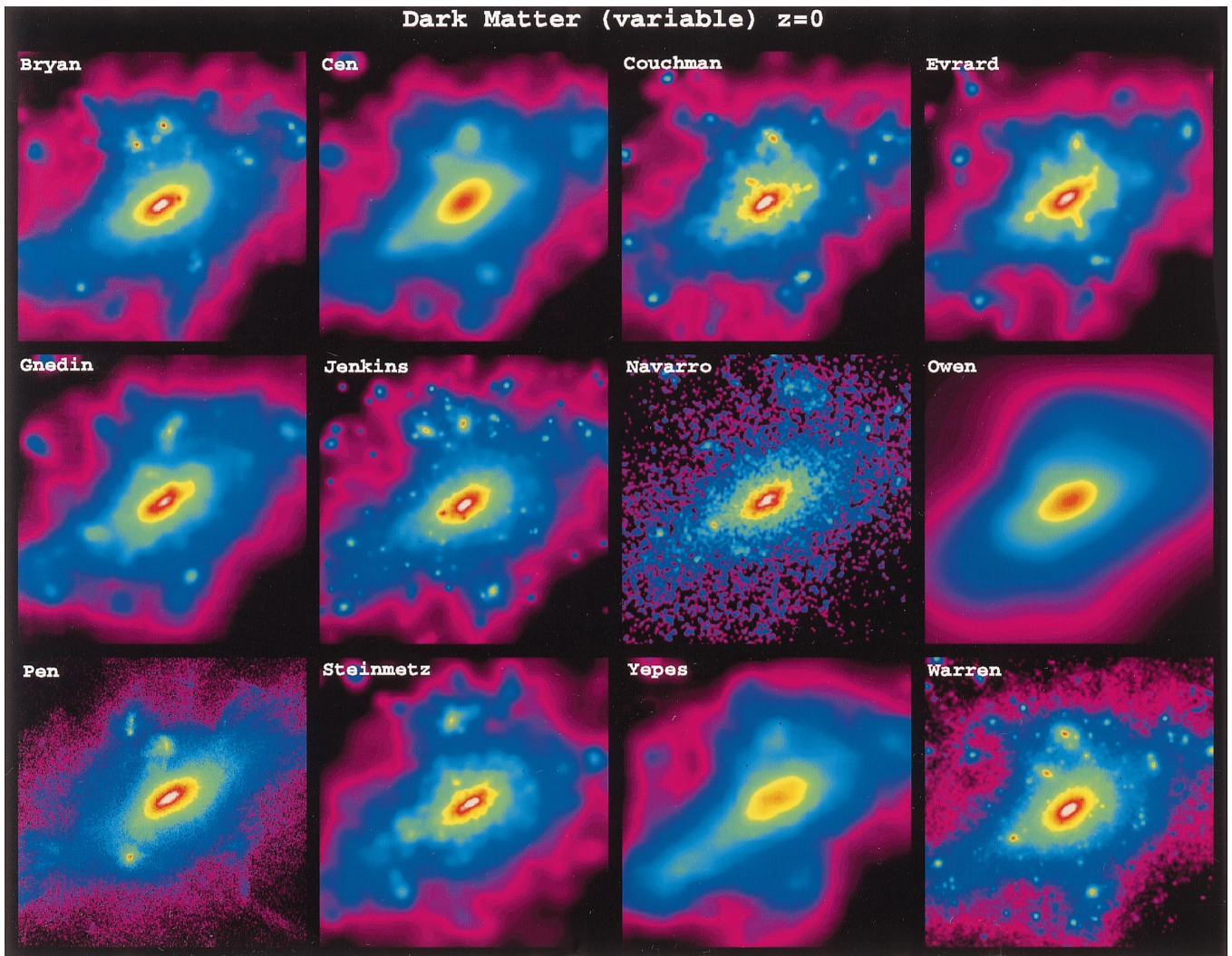
Fig. 8.—Projected dark matter density at $z = 0$. The images, covering the inner 8 Mpc of each simulation cube, have been smoothed with the filter chosen by each author to best portray the results of each simulation (see Table 1).

ably because of the relatively large contribution to $\mathscr{I}$ from the largest infalling clump that lies close to r_{200} in his simulation. Gnedin's dark matter and gas distributions are considerably more aspherical than the rest.

4.3. Radial Profiles

In order to perform more detailed quantitative comparisons of cluster structure, each simulator was asked to provide the radial profiles of a number of cluster properties. These were averaged in a specified set of spherical shells centered at the position deemed by each simulator to be the cluster center (cf. § 2.2). Simulators were also asked to specify the effective resolution of their simulation, and throughout this section we plot data for each model only at radii larger than this. Most simulators identified the resolution of their simulation with the effective gravitational force resolution (see Table 1), but the following specified different values: Cen (200 kpc), Owen (500 kpc), Pen (50 kpc), Steinmetz (35 kpc), and Yepes (400 kpc). In the figures that follow, the data points are slightly displaced from the bin centers for clarity, and we use a solid line to show the mean profile obtained by averaging all the data plotted in

each bin. At the top of each diagram we plot the residuals from this mean, defined in most cases as $\ln x - \langle \ln x \rangle$, where x is the property of interest and the brackets denote the average of the data points in each bin. This definition applies to the residuals of all the radial profiles, except those of the normalized baryon fraction (Fig. 13), which we define as $(x - \langle x \rangle)/\langle x \rangle$, and those of the radial velocity profiles (Figs. 14 and 15) and the entropy (Fig. 18), which we define as $x - \langle x \rangle$. The sampling errors in the estimates of the different cluster properties are largest in the innermost bin plotted where they are typically less than about 10%.

We begin by comparing the dark matter density profiles plotted in Figure 10. In general there is very good agreement between the different calculations over the regions resolved by each simulation. The two highest resolution models, Warren's pure N-body simulation and Jenkins' AP^{3}M/SPH simulation, agree extremely well at all radii. The residuals plot shows that all simulations agree to within $\pm 20\%$ at all radii. The dark matter profile in this cluster is well fit by the analytic form proposed by Navarro, Frenk, & White (1995), all the way from 10 kpc to 10 Mpc. This fit is shown as a dashed line in Figure 10 and corresponds to a
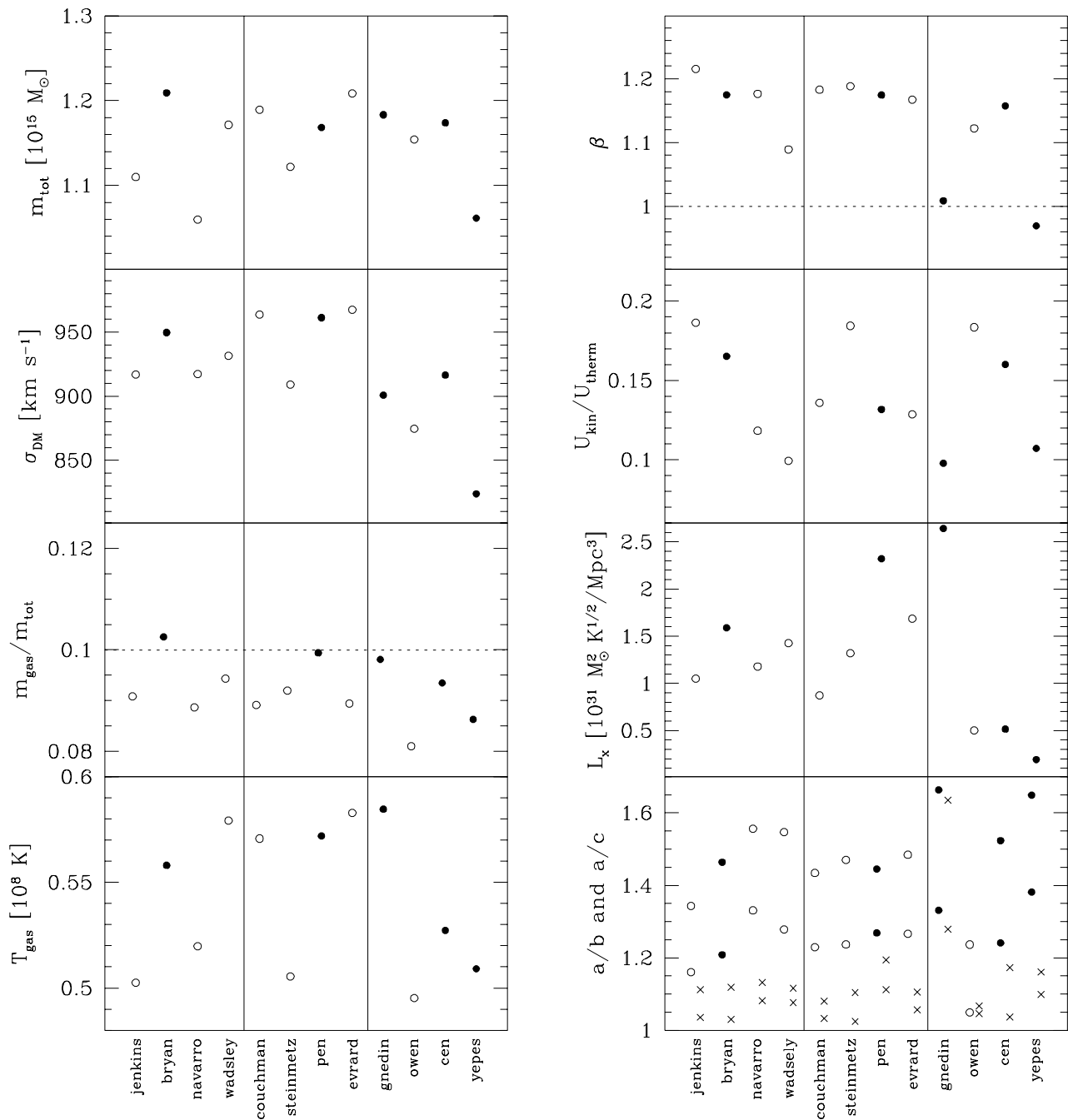
FIG. 9.—Global properties of the cluster in the various simulations. All quantities are computed within the virial radius. From top to bottom, the left column gives the values of: (a) the total cluster mass; (b) the one-dimensional velocity dispersion of the dark matter; (c) the gas mass fraction; (d) the mass-weighted gas temperature. Also from top to bottom, the right column gives the values of: (a) $\beta = \mu m_p \sigma_{dm}^2 / 3kT$; (b) the ratio of bulk kinetic to thermal energy in the gas; (c) the X-ray luminosity; (d) the axial ratios of the dark matter (circles) and gas (crosses) distributions. In each panel, the models are arranged, from left to right, in order of decreasing resolution, which is taken to be the maximum of the spatial resolution for the gas at cluster center (col. [4] of Table 1) and the gravitational softening length (col. [7] of Table 1). Open circles are used to represent SPH simulations and filled circles grid based simulations.

value of the concentration parameter, $c = 7.5$, appropriate to a typical isolated halo of this mass in an $\Omega = 1$ CDM model (Navarro, Frenk, & White 1997). Only in the very center is there a slight indication that the true profile, as defined by Warren's model, might be steeper than the analytic form.

The dark matter velocity dispersion profiles in Figure 11 confirm that all the codes give very similar results for the dynamical properties of the dark matter. (Note the very

different dynamic ranges in Figs. 10 and 11.) Except for the last bin, which is particularly affected by noise arising from subclustering, the scatter in the velocity profiles is comparable to that in the mass profiles, about 20%. The velocity dispersion profile rises near the center, has a broad peak around 100–500 kpc, and declines in the outer parts. Warren's N-body model and all the high-resolution SPH and grid models resolve the inner rising part of the velocity dispersion profile.
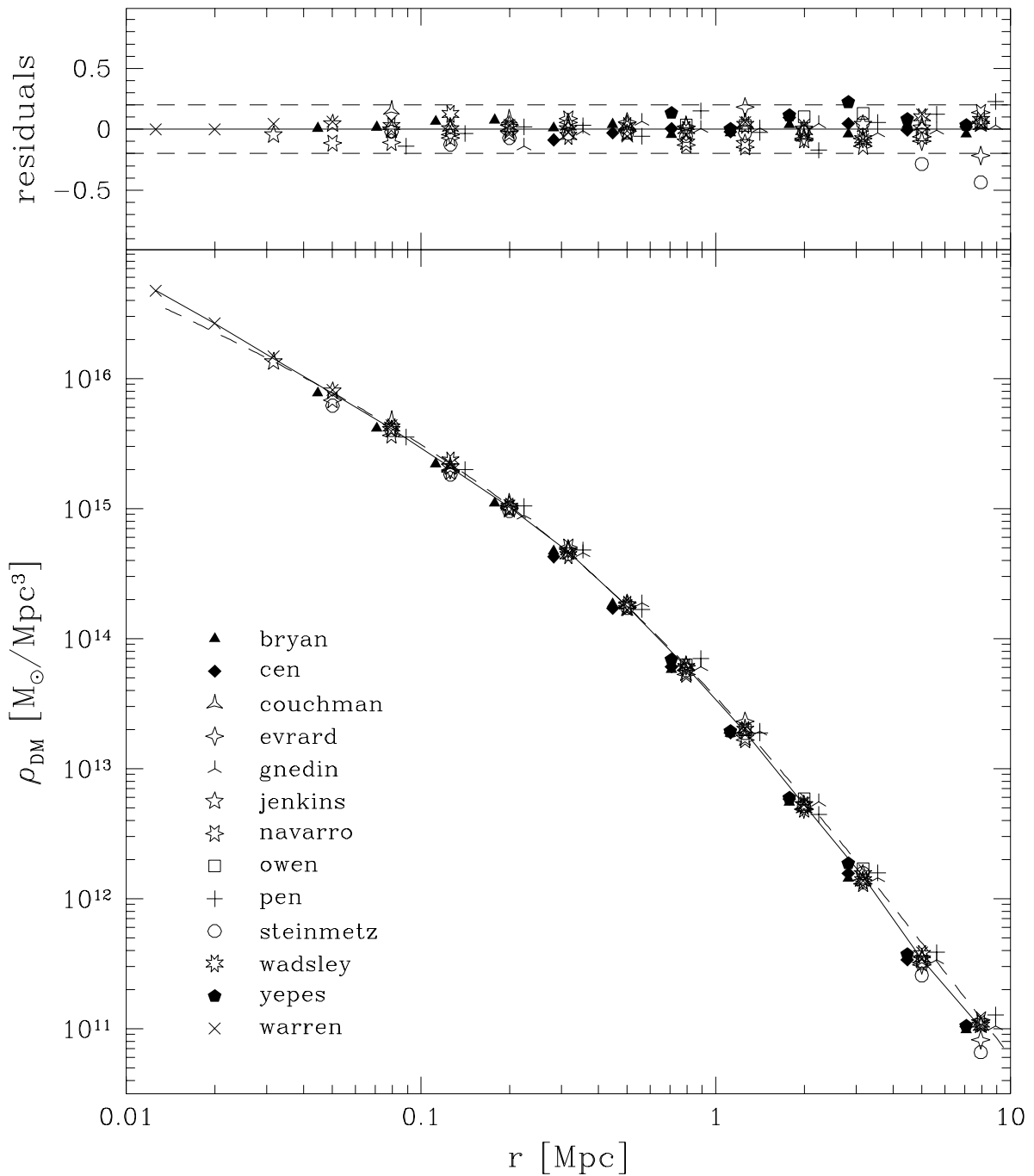
FIG. 10.—Dark matter density profile. The main plot shows the spherically averaged profile, calculated about the point deemed by each simulator to be the cluster center. Some of the data points are slightly displaced from the bin center for clarity. Data are plotted only at radii larger than the effective resolution quoted by each simulator. The solid line shows the mean profile obtained by averaging the data plotted in each bin. The dashed line shows the analytic model proposed by Navarro et al. (1995), with the value of the concentration parameter, $c = 7.5$, appropriate to a typical isolated halo of this mass in an $\Omega = 1$ CDM model (Navarro et al. 1997). The diagram at the top shows the residuals from the mean profile, defined as $\ln \rho_{dm} - \langle \ln \rho_{dm} \rangle$, where the brackets denote the average for each bin.

The agreement of the gas density profiles (Fig. 12) is less good but is still quite impressive. In the fixed Eulerian grid models of Cen and Yepes, the gas density at their innermost point is somewhat low, whereas the corresponding dark matter densities agree well with the other calculations. This shows, unsurprisingly, that the resolution of such codes is somewhat poorer for the hydrodynamics than for the N-body dynamics. Bryan's multilevel grid code produces results that agree quite well with other high-resolution models, except that his two innermost points lie slightly below those of the highest resolution SPH models. Gnedin's and Pen's variable resolution grid codes give higher than average gas densities in the 200–600 kpc range and, as a result, their density profiles are steeper than the others. Pen's simulation produced a more pronounced core structure within about 150 kpc than all other models while Gnedin's simulation shows the largest departures from the mean profile. There is also significant scatter among the
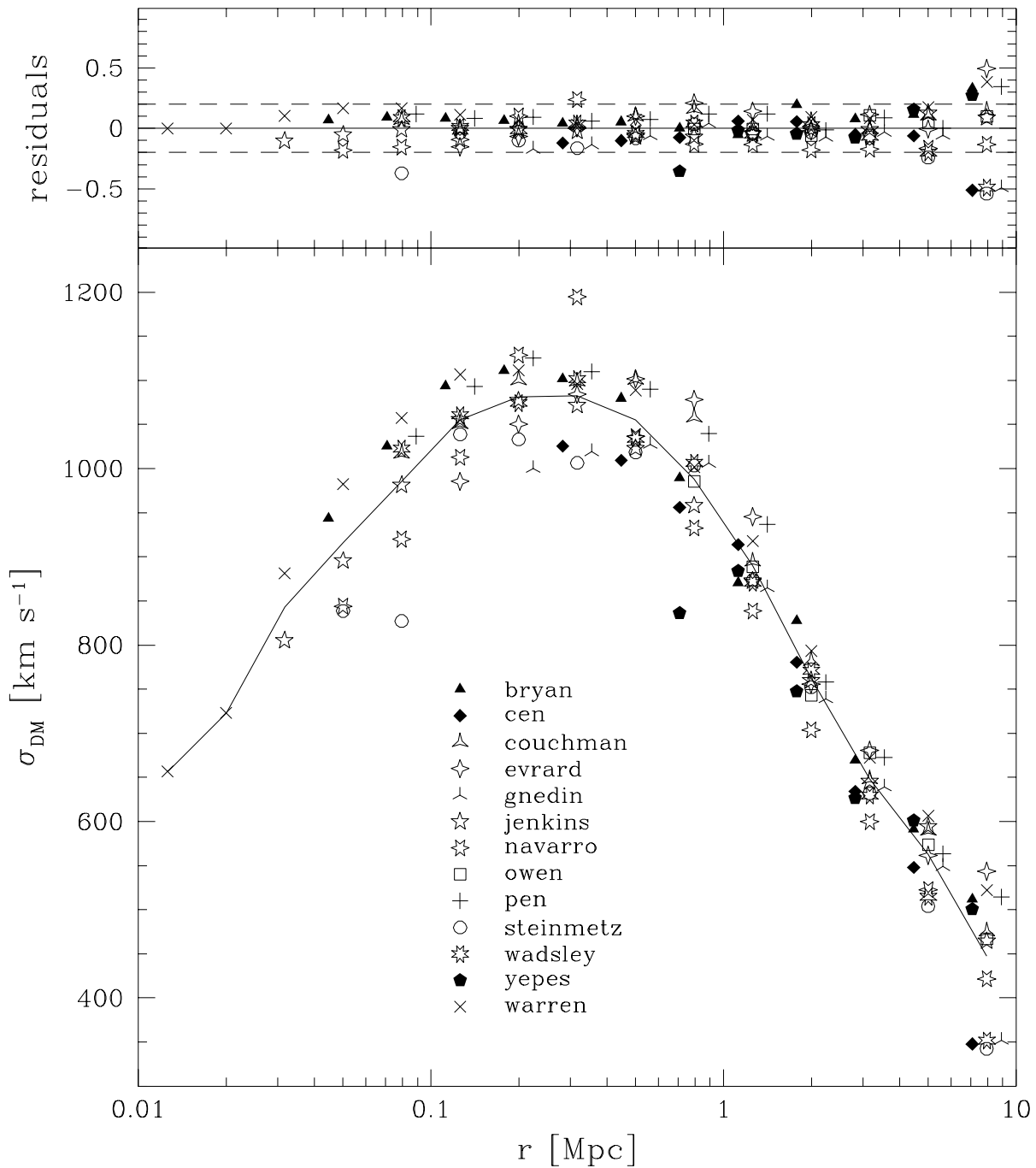
Fig. 11.—Dark matter velocity dispersion profile. The quantity shown in the main plot is the one-dimensional velocity dispersion, calculated as $\sigma/\sqrt{3}$, where σ is the full three-dimensional velocity dispersion. See legend to Fig. 10 for a description of the symbols and other details of the plot.

results of the various SPH codes, Evrard finding systematically high gas densities in the inner cluster and Couchman finding systematically low values. It seems likely that at least some of these differences result from the differences in the timing of cluster collapse noted in § 4.1, rather than from differences in the treatment of the hydrodynamics between the different techniques and implementations although the two cannot be clearly disentangled. For example, Couchman's gas densities between 80 and 200 kpc are somewhat lower than those obtained by Jenkins using the same SPH implementation but different numbers of particles and integration parameters. The dashed line in Figure 12 is the

mean dark matter density profile reproduced from Figure 10. It is interesting that this profile is substantially steeper than the mean gas density profile in the inner cluster, indicating that the gas has developed a much more clearly defined " core " than the dark matter.

The discrepancies between the various dark matter and gas density profiles become clearer when we examine the variation of the normalized gas fraction, $\Upsilon = M_{\mathrm{gas}}(<r)/[\Omega_b M_{\mathrm{tot}}(<r)]$, with radius (Fig. 13). There is considerable scatter ($\sim 50\%$) in this gas fraction over the 100 kpc to 1 Mpc range, Gnedin finding the highest values and Couchman, Cen, and Yepes the lowest. Well inside the virial
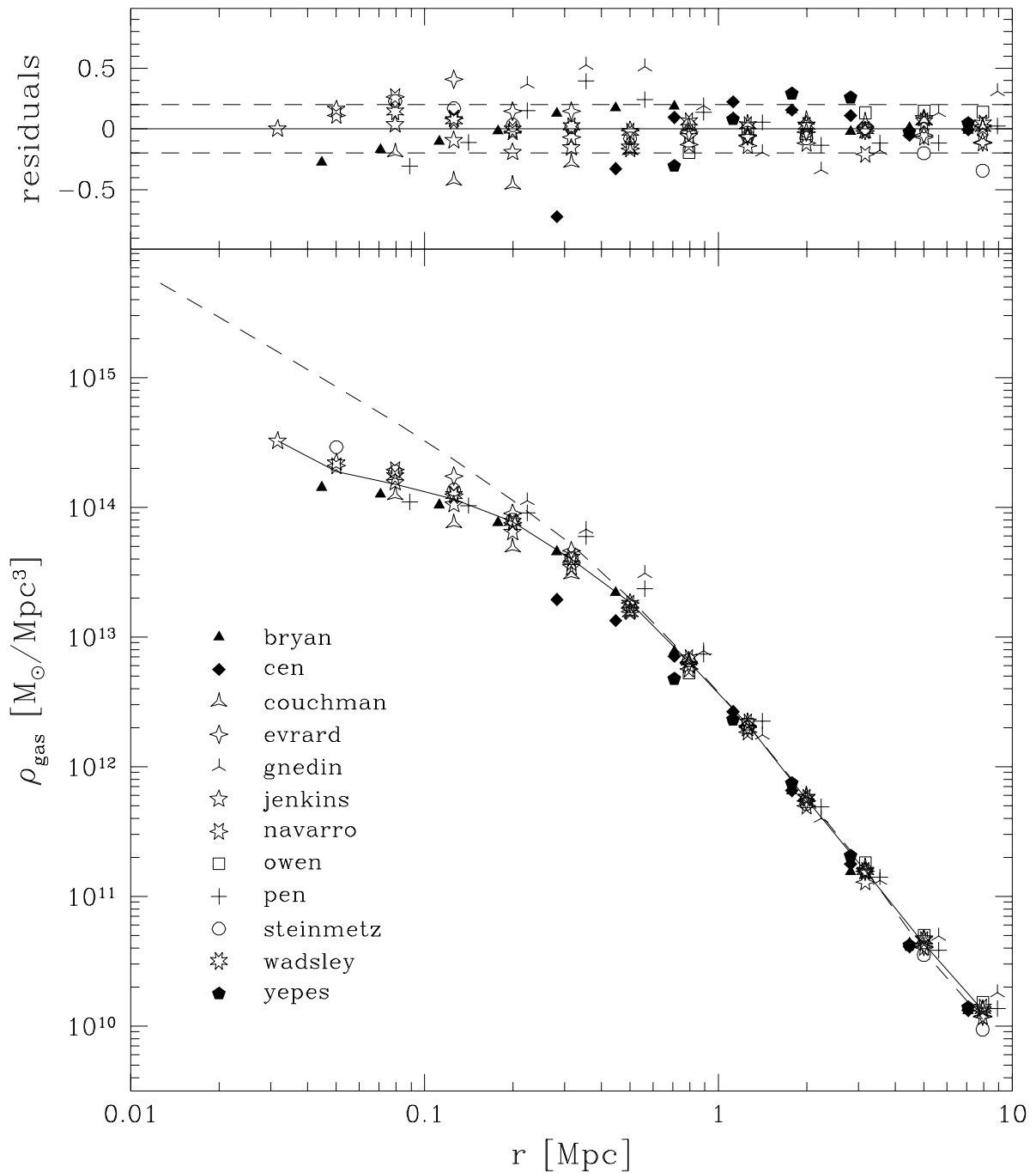
FIG. 12.—Gas density profile. The dashed line shows the mean dark matter density profile reproduced from Fig. 10. See legend to Fig. 10 for further details.

radius, three of the grid models, Bryan's, Pen's, and especially Gnedin's, rise above $\Upsilon = 1$, the mean for the simulation as a whole. At larger radii, Pen's values fall slightly below this mean, while Bryan's and Gnedin's remain slightly above unity well beyond the virial radius. By contrast, none of the SPH models ever rise above $\Upsilon = 1$, and they all give very similar results at the virial radius, similar also to the Eulerian models of Cen and Yepes. Although relatively small, these discrepancies appear to reflect a systematic difference in the final distribution of the gas between the three intermediate- and high-resolution grid simulations (Gnedin, Pen, and Bryan) and the rest of the models. Particularly

puzzling is the excursion toward large values of Υ seen by Gnedin at $r \simeq 1$ Mpc and the fact that Bryan and Gnedin obtain values of $\Upsilon > 1$ beyond three virial radii where one might expect the mixture of dark matter and gas to attain the mean universal value. Note, however, that the deviations from $\Upsilon = 1$ at large radii are quite small.

The infall patterns of dark matter and gas around the cluster (i.e., the run of peculiar radial velocities) are illustrated in Figures 14 and 15. For the dark matter, the radial velocity profiles are quite similar: net infall is seen in most models beyond ~ 700 kpc, except in Pen's case, in which the radial velocity remains close to zero until about twice this
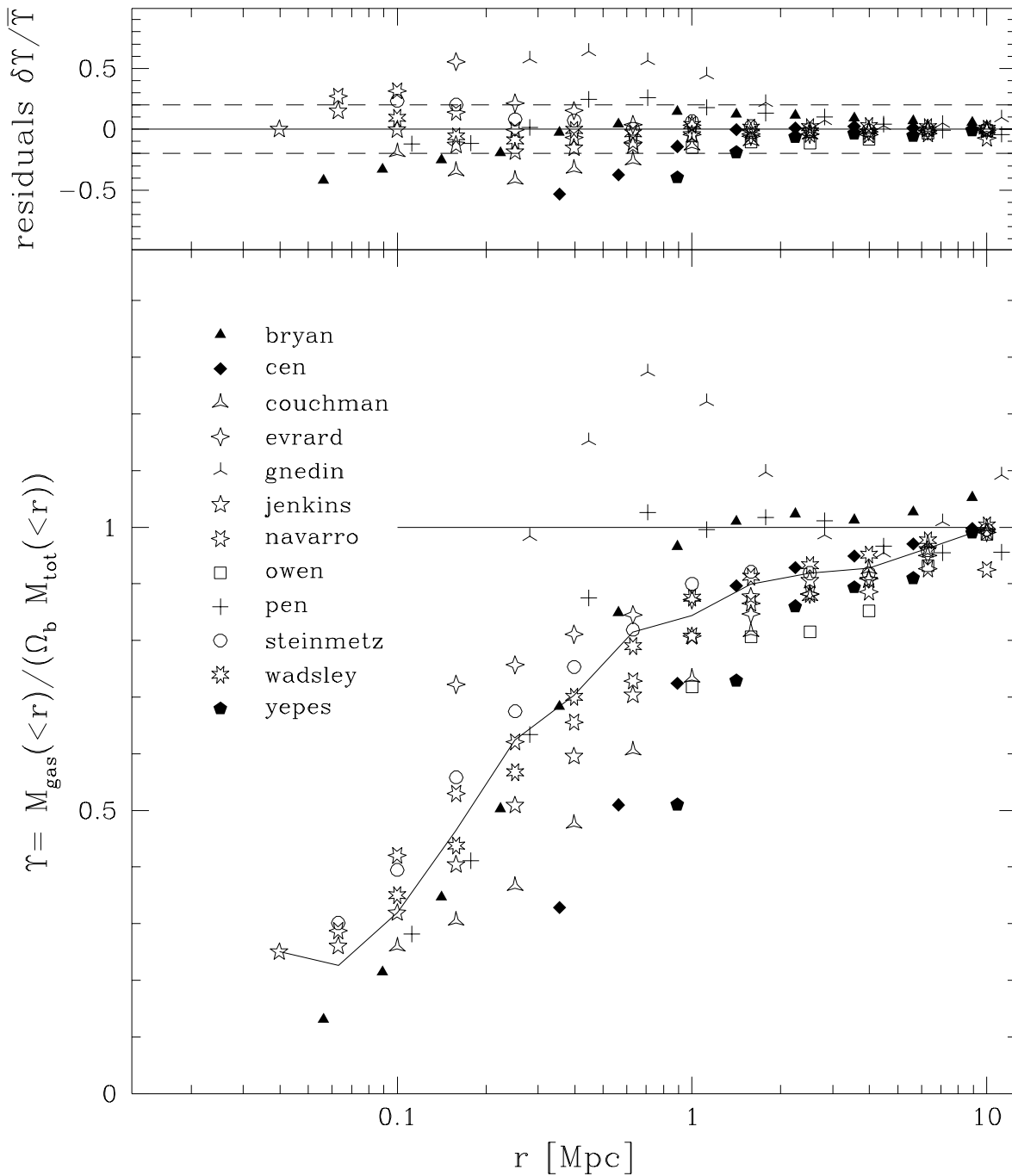
FIG. 13.—Radial dependence of the gas fraction. The quantity plotted is the gas fraction normalized to the value for the simulation as a whole (10%). See legend to Fig. 10 for further details, but note that in this figure residuals are defined as $(\Upsilon - \langle\Upsilon\rangle)/\langle\Upsilon\rangle$.

radius. There are larger differences in the radial velocity profiles for the gas. In most models the gas is infalling over the same range of radii as the dark matter, but at a slightly lower speed. Gnedin's model is anomalous in this respect. In Pen's simulation, on the other hand, there is a small net outflow of gas at ~ 1 Mpc. The scatter in the radial velocity profiles beyond ~ 1 Mpc is about 200 km s^{-1}.

The differences between the codes become most obvious when we look at various thermodynamic properties of the gas. Figures 16, 17, 18, and 19 show radial profiles for the pressure, temperature, entropy, and X-ray emissivity. (Of these, only the temperature was calculated directly by the

simulators; the other quantities were derived from the binned values of temperature, density, and X-ray luminosity.) Agreement among the pressure profiles is reasonably good. This reflects the good agreement of the dark matter density profiles and so of the gravitational potential wells, together with the fact that the intracluster gas is close to hydrostatic equilibrium in all cases. In the central regions, simulations that give flatter gas density profiles (e.g., Bryan, Pen, Couchman, and Cen) can be clearly seen to give correspondingly higher temperatures, as required in order to maintain comparable pressure gradients. The differences in the temperature profiles appear substantially
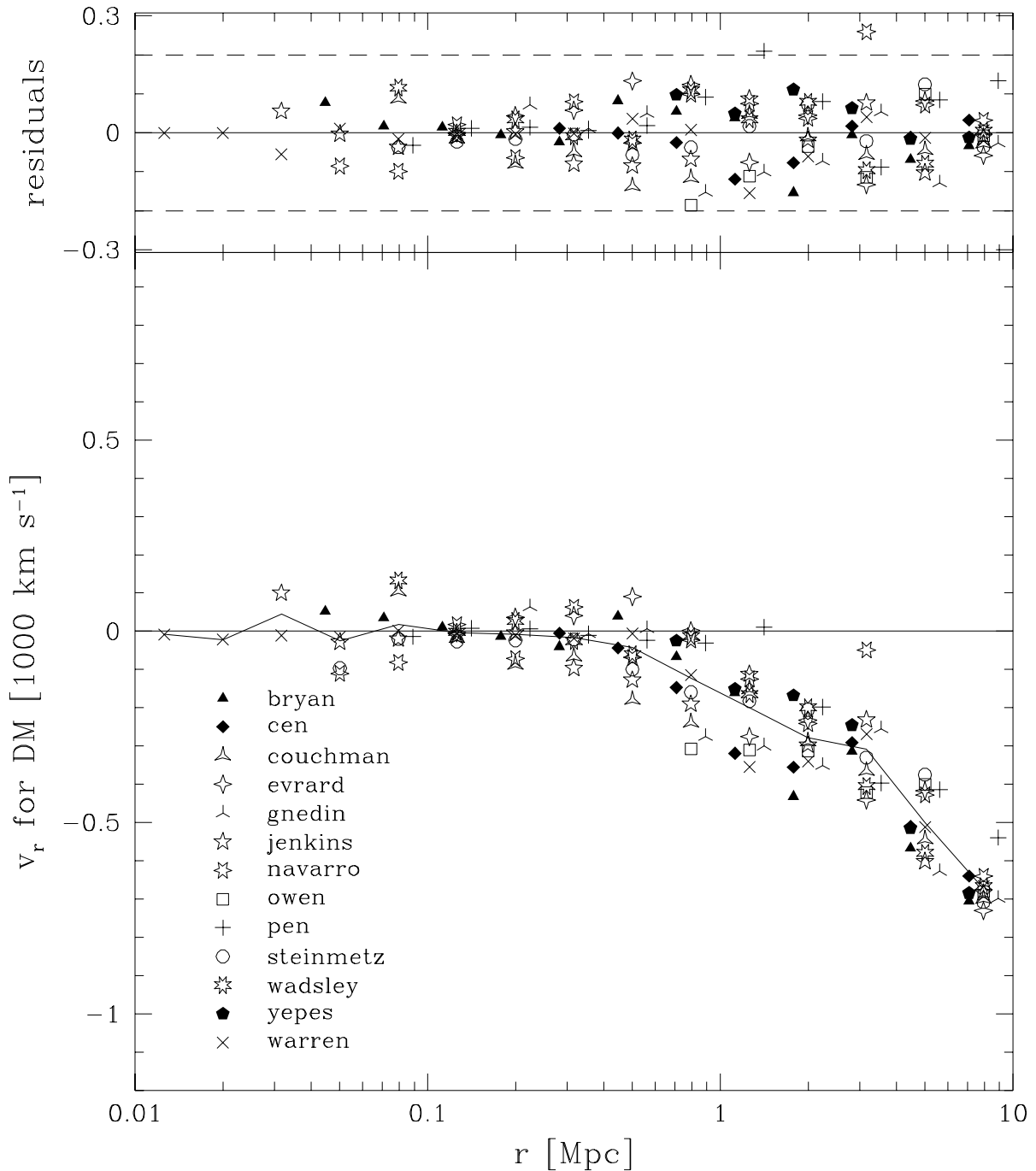
FIG. 14.—Radial velocity profile of the dark matter. Velocities are computed in the rest frame of the cluster and do not include the Hubble expansion. See legend to Fig. 10 for further details, but note that in this figure the residuals are defined as $v_r - \langle v_r \rangle$.

larger than in other quantities, but this is in part a reflection of the smaller dynamic range of the plot. There is a suggestion that the temperature structure in the inner parts may be systematically different in the SPH and grid models. In the former, the temperature profile is flat or slowly declining toward the inner regions, but, in the grid simulations, the temperature is still rising at the innermost point plotted, a trend that is particularly noticeable in Bryan's simulation. In the outer cluster, the temperature profile drops substantially in all cases.

The entropy and X-ray luminosities show the patterns expected for quantities derived in a simple way from the density and temperature of the gas. Note, in particular, that the entropy [defined as $s = \ln(T/\rho_{\rm gas}^{2/3})$] decreases systematically toward the center in all the SPH models, but that this decline is less obvious in the grid models and is, in fact, absent in the central parts of Bryan's simulation, in which the entropy remains approximately constant within ~ 200 kpc. This difference might reflect differences in the way in which shocks are treated in the SPH and grid codes; however, the effect is small and occurs at the resolution limit of the grid simulations. Finally, Figure 19 shows the contribution to the total X-ray luminosity per logarithmic interval in radius, $4\pi r^3 \mathscr{L}_{\rm X}$. Most of the X-ray luminosity is
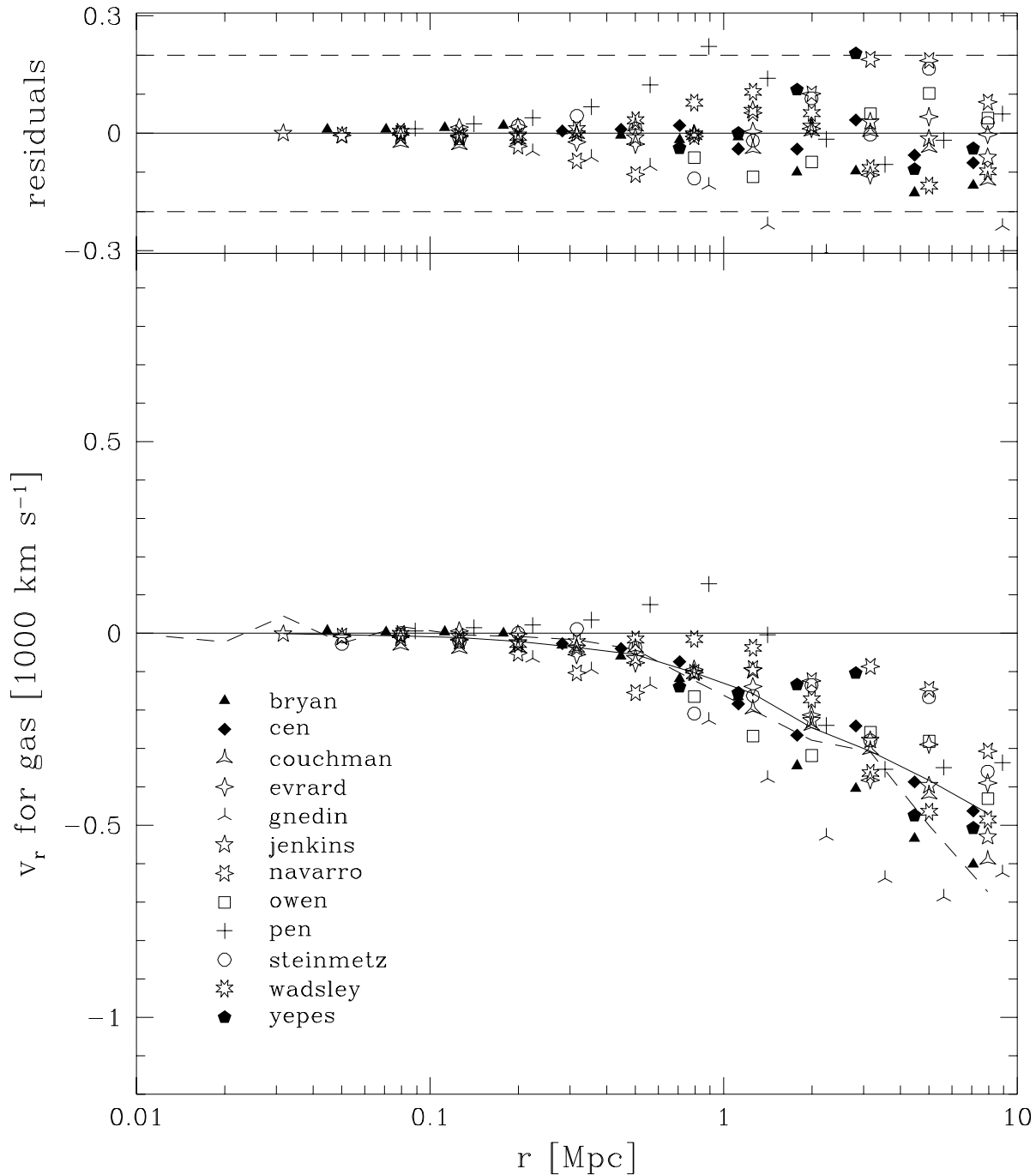
FIG. 15.—Radial velocity profile of the gas. Velocities are computed in the rest frame of the cluster and do not include the Hubble expansion. The dashed line is the dark matter radial velocity profile from Fig. 14. See legend to Fig. 10 for further details, but note that in this figure the residuals are defined as $v_r - \langle v_r \rangle$.

produced in the radial range 200–500 kpc. This region was well resolved by all the SPH simulations and by Bryan's model, which agrees remarkably well with them. On the other hand, Cen, Owen, and Yepes did not resolve this radial range and, as a result, their total luminosities ended up being smaller than average. The large gas densities found by Gnedin and Pen in this range account for their larger than average total luminosities (see Fig. 9). Thus, the large scatter in total X-ray luminosity seen in Figure 9 results partly from the low resolution of some of the models and partly from the unusually high gas densities found by the two deformable grid models. Between ∼1 Mpc and the

virial radius the different models agree better although the scatter in $4\pi r^3 \mathscr{L}_X$ is still larger than in all other properties.

5. DISCUSSION AND CONCLUSIONS

We have simulated the formation of an X-ray cluster in a cold dark matter universe using 12 different cosmological gasdynamics codes that span the range of numerical techniques and implementations presently in use. This comparison aims to assess the reliability of current cosmological simulations in the regime relevant to the bulk of the gas in galaxy clusters, and to set a standard against which future
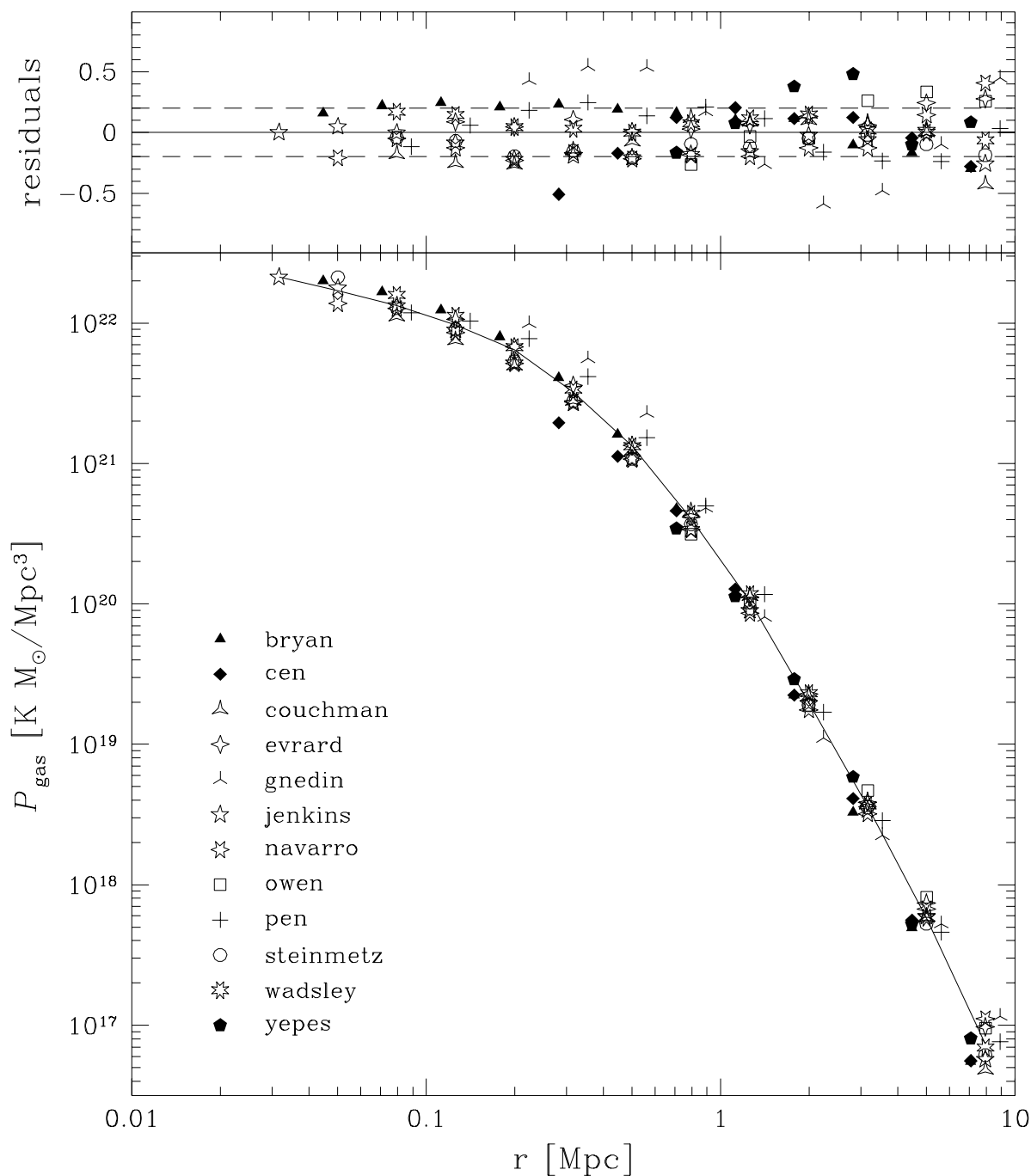
FIG. 16.—Gas pressure profile. See legend to Fig. 10 for further details.

techniques may be tested. (The initial conditions and a selection of results are available over the Internet[24] or by request from C. S. F.) Because our goal is to compare results in a realistic situation, only the initial conditions were specified. Other variables such as resolution, the treatment of boundary conditions, and integration parameters were left to the discretion of simulators. Our comparison therefore encompasses not only the current variety of hydrodynamics techniques, but also the different choices commonly made by individual authors for these variables. Seven of the codes

used for this comparison are based on the SPH technique, while the other five are based on grid methods, employing either a fixed, a deformable, or a multilevel mesh. The resolution of the simulations varied from a few tens to a few hundreds of kiloparsecs. Although there is, of course, no guarantee that any of the calculations gives the correct solution to the problem, the agreement among the various simulations was better than a pessimist might have predicted. Nevertheless, some important differences do exist.

The simulated cluster was chosen to have a mass comparable to the Coma cluster at the present day and to appear fairly relaxed on visual inspection. We assumed cold dark matter initial conditions, $\Omega = 1$, $h = 0.5$, and a global

[24] Available at http://star-www.dur.ac.uk/ csf/clusdata/.
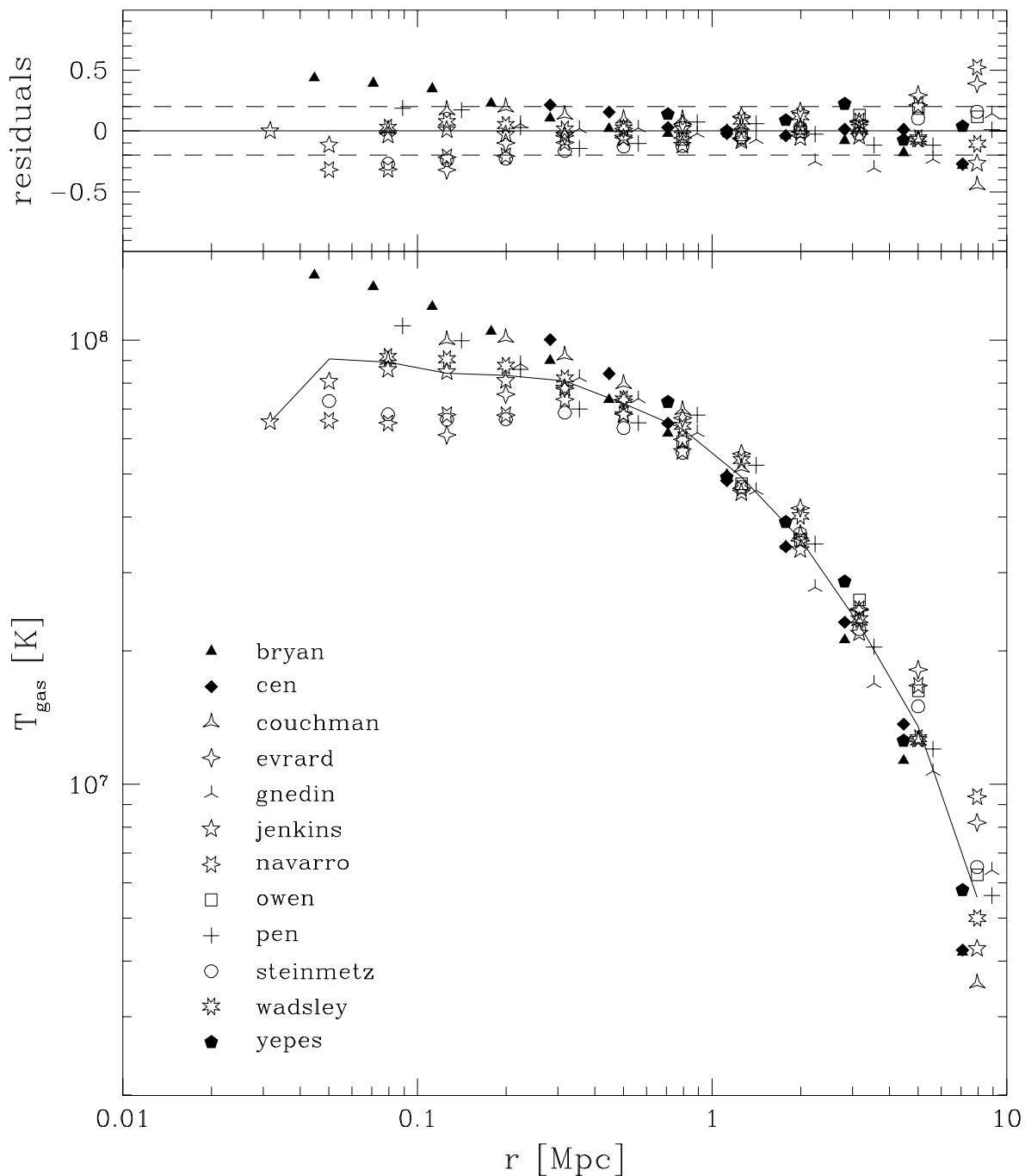
FIG. 17.—Gas temperature profile. The quantity plotted is the mass-weighted temperature. See legend to Fig. 10 for further details.

baryon fraction of 10%. The cluster formed by the merging of subclumps infalling along a filament and experienced a final major merger between $z = 0.5$ and $z = 0$. The final cluster mass, virial radius, gas fraction within the virial radius, and mass-weighted gas temperature, averaged over all the simulations, and the standard deviation in each quantity are $M = 1.1 \times 10^{15} \ M_{\odot}$, $\sigma_M = 0.05 \times 10^{15} \ M_{\odot}$; $r_v = 2.70$ Mpc, $\sigma_{r_v} = 0.04$ Mpc; $f_b = 0.092$, $\sigma_{f_b} = 0.006$; and $T = 5.4 \times 10^7$ K, $\sigma_T = 0.34 \times 10^7$ K, respectively.

The properties of the cluster dark matter are gratifyingly similar in all the models. The total mass and velocity dispersion agree to better than 5%. The dark matter density and velocity dispersion profiles are also similar and match the

result of a higher resolution dark matter only simulation. Over the regions adequately resolved in each simulation, the scatter in these quantities, relative to the mean profile, is less than about $\pm 20\%$ per logarithmic bin in radius. For the most part, this scatter seems to be due to a slight asynchrony in the evolutionary state of the models introduced by inaccuracies in the initial conditions, the treatment of boundary conditions and of tidal forces and the integration procedure. Thus, small subclumps often appear at different positions and the timing of the final major merger differs slightly in the different models.

There is less agreement on the gas properties of the cluster, although in most cases they are quite similar. For
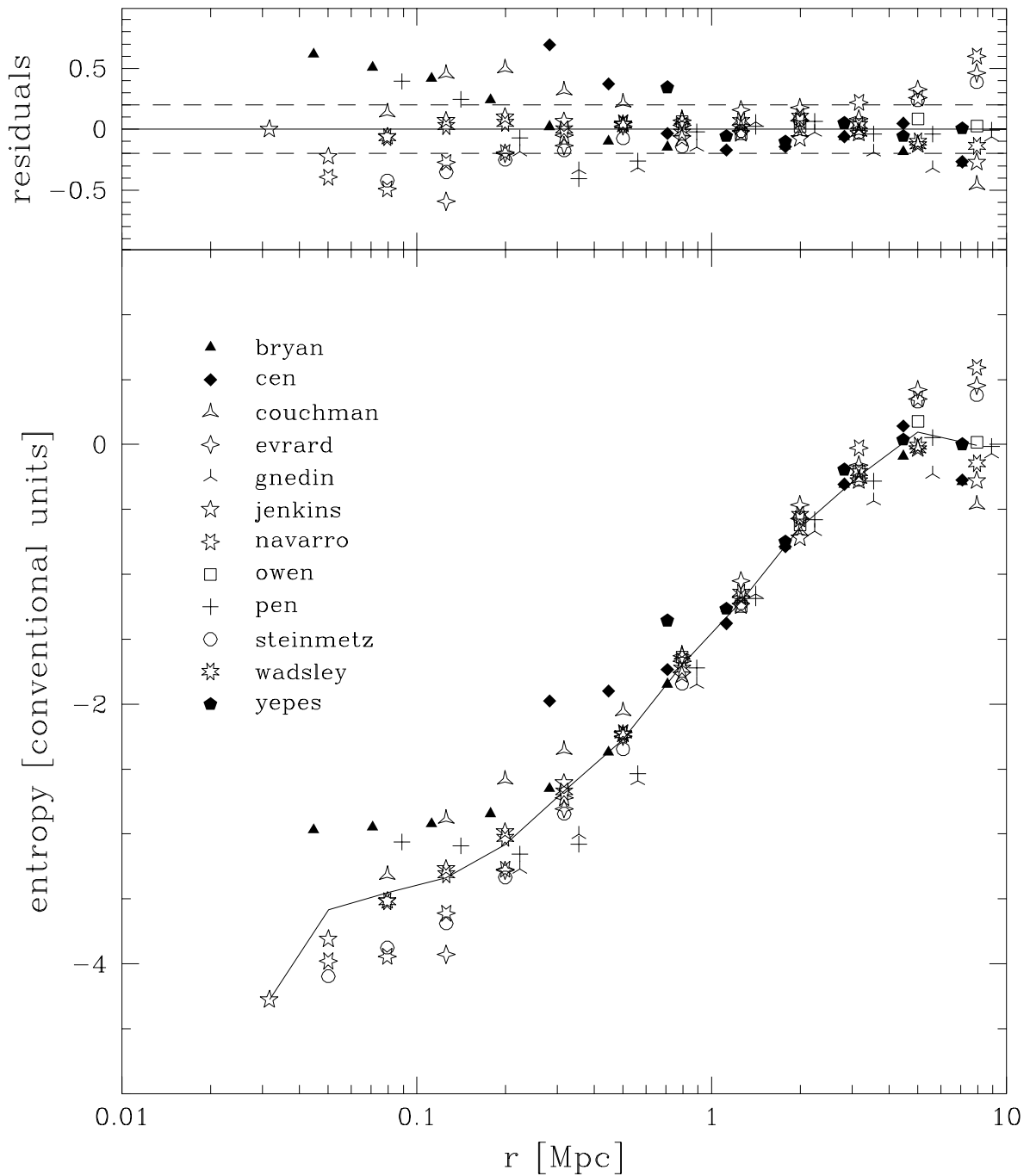
FIG. 18.—Radial variation of the gas entropy. The entropy is defined as $s = \ln(T/\rho_{gas}^{2/3})$. See legend to Fig. 10 for further details.

example, all models agree to 10% (rms) on the gas mass and baryon fraction within the virial radius. In all the SPH and all but one of the grid models, the gas is slightly more extended than the dark matter. The scatter relative to the mean in logarithmic radial bins seldom exceeds 20% in the case of the density profile and 30% in the case of the gas mass fraction. There is no obvious systematic difference in the gas density profiles produced by the SPH and fixed grid models, but the deformable grid models produced somewhat larger core radii. At large distances from the cluster, some of the grid based models rise slightly above the theoretical expectation of a universal baryon fraction.

The mean (mass-weighted) gas temperature is reproduced to within 6% (rms) by all the codes. The ratio of specific dark matter kinetic energy to gas thermal energy is reproduced to a similar accuracy. The scatter per logarithmic bin in the temperature profiles falls in the ±20% band and is only slightly larger for the pressure profile. In the central regions ($r \leq 100\,\mathrm{kpc}$), however, the SPH codes produce a flat or slightly declining temperature profile while all the grid codes produce a temperature profile that is still rising at the resolution limit. The entropy of the gas declines continuously from the virial radius to the resolution limit, but there is a suggestion that the entropy in the grid codes may
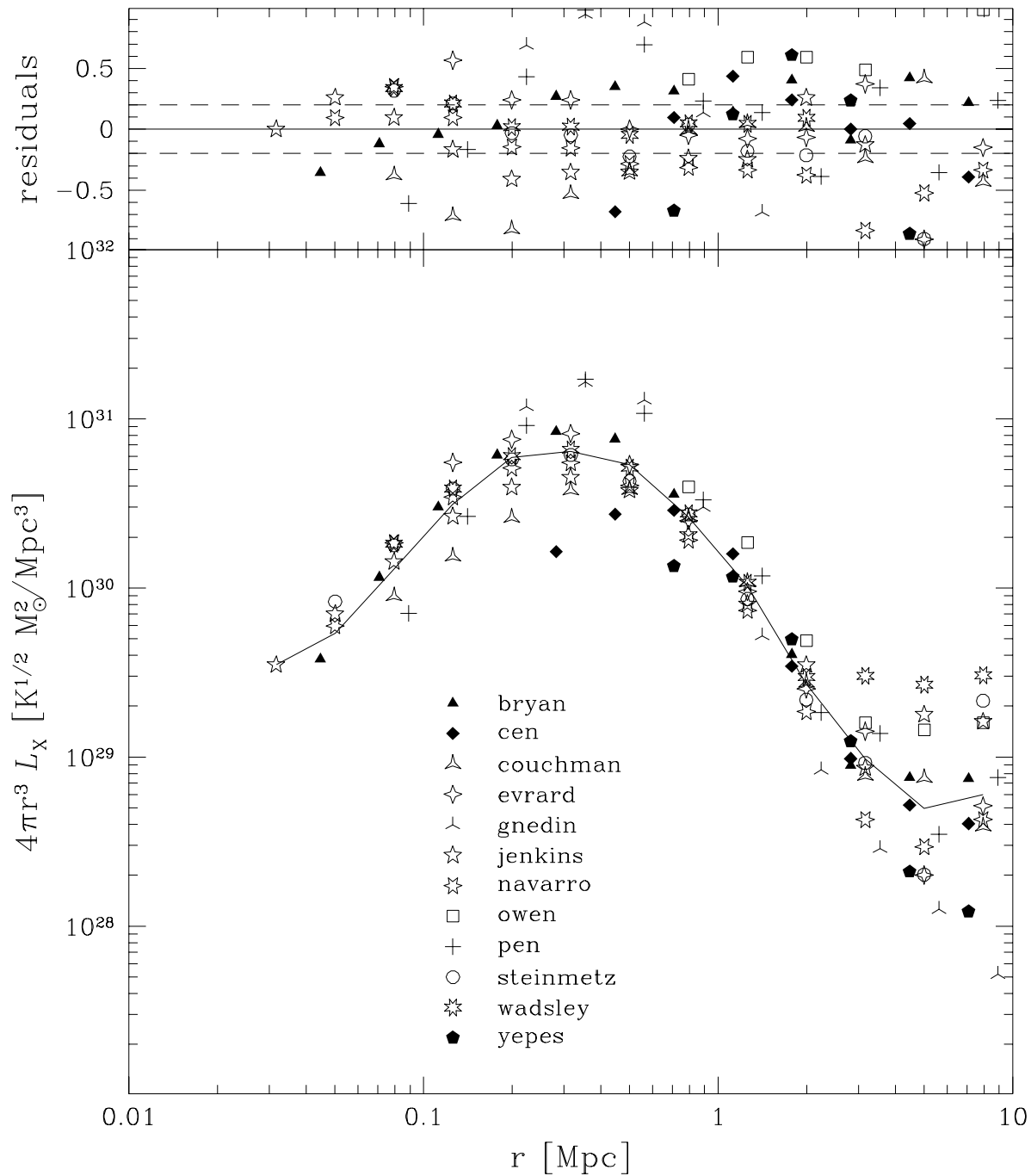
Fig. 19.—X-ray luminosity profile. The quantity plotted is $4\pi r^3 \mathscr{L}_X$, where $\mathscr{L}_X$ denotes the X-ray luminosity density in each bin. See legend to Fig. 10 for further details.

bottom out at small radii while it continues to decrease in the SPH codes.

Among all the properties we have examined, the largest discrepancies occur in the predicted cluster X-ray luminosity. This is proportional to the square of the gas density and so is strongly dependent on resolution and is further affected by variations in the potential produced by the exact timing of the final major merger. The large range of effective resolution in the various models gives rise to a factor of 10 variation in the total X-ray luminosity. The luminosity per logarithmic interval in radius peaks just outside the gas core radius. The eight simulations that resolved this region (all the SPH and two of the grid models) show a much narrower

spread in total X-ray luminosity, amounting to a factor of 2.6 (or 1.8 if the most extreme model is excluded.)

We conclude that the different approaches to modeling shocks and other hydrodynamical processes implicit in the diverse techniques employed in this comparison give, in most cases, fairly consistent results for the dynamical and thermodynamical properties of X-ray clusters. Variations introduced by differences in the internal timing of the simulations tend to be at least as important as variations in the treatment of hydrodynamics. An illustration of this is the comparison of the simulations of Couchman and Jenkins, who used serial and parallel versions of essentially the same code but with different numbers of particles and other simu-

lation parameters. The final temperatures of their clusters differed by 15%, the X-ray luminosities by 20%, and the bulk gas kinetic energy by 15%.

The conclusions discussed in this paper apply exclusively to the particular case of a nonradiative gas. They cannot be extrapolated to other regimes such as that appropriate to galaxy formation where gas cooling is a dominant process. The behavior of the gas in this situation is determined by the resolution of the simulation because the cooling rate depends strongly on gas density. In addition, simulations of galaxy formation often include algorithms to convert cold gas into stars and to model the feedback processes associated with star formation. A comparison of galaxy formation simulations analogous to the comparison of X-ray cluster formation carried out in this paper is clearly desirable but would be much more complex to implement in practice. The level of agreement among the techniques currently in use for studies of galaxy formation remains an open question. Perhaps a simpler, but instructive, next step might be a comparison of simulations of high-redshift gas clouds (the "Lyα forest" clouds), in which gas cooling is less important.

Based on the overall consistency of the simulations discussed in this paper, we can draw a number of conclusions regarding the properties of the simulated cluster, which we expect to be typical of near equilibrium, massive clusters in a CDM universe. Some of these conclusions mirror those found in earlier work (e.g., Evrard 1990; White et al. 1993; Bryan et al. 1994; Cen & Ostriker 1994; Kang et al. 1994a; Navarro et al. 1995; Anninos & Norman 1996; Bartelman & Steinmetz 1996).

1. The dark matter distribution in our simulated cluster is elongated along the direction of the dominant large filament along which subclumps were accreted onto the cluster. The final gas distribution is rounder than the dark matter distribution, and, as a result, the direction of the filament is difficult to identify in an X-ray image.

2. The dark matter density profile in the cluster is well fit by the analytic form proposed by Navarro et al. (1995), all the way from 10 kpc to 10 Mpc. This form has a radial dependence close to r^{-1} in the inner regions, steepens to r^{-2} at intermediate radii, and falls off as r^{-3} in the outer parts. The corresponding velocity dispersion profile rises from the center outward, has a broad maximum around 100–500 kpc, and declines in the outer parts.

3. Although the gas is close to hydrostatic equilibrium throughout the cluster, mergers disturb both the gravitational potential and the dynamical state of the gas. Bulk motions make a small but significant contribution to the support of the gas: the kinetic energy in bulk gas motions is about 15% of the thermal energy of the gas. The quantity $\beta = \mu m_p \sigma_{dm}^2 / 3kT$ has a mean (averaged over all the simulations except the lowest resolution one) of 1.15 with an rms scatter of only 0.05.

4. The radial density profile of the gas in the highest resolution simulations develops a "core radius," i.e., a region in which the slope of the profile flattens rapidly. This change of slope occurs at $r \lesssim 250$ kpc, and, inside this radius, the gas density profile is significantly flatter than the dark matter density profile. The gas fraction within a given radius therefore rises from the center outward, and, at the virial radius, the mean over all the simulations is 0.92 of the global value, with a fractional rms scatter of only ± 0.065. The temperature distribution in the inner parts has an approximately flat profile, and, beyond a few hundred kpc, it begins to decline so that, at the virial radius, the temperature is $\sim 30\%$ of the central value.

5. A reliable estimate of the cluster X-ray luminosity requires resolving the radial range 200–500 kpc, or 5%–20% of the virial radius, where the X-ray luminosity per logarithmic interval in radius peaks. Even when this is possible, the strong sensitivity of X-ray luminosity to local variations in gas density leads to a spread of a factor of ~ 2 in the predicted X-ray luminosity. These variations are due to a variety of numerical effects, and a factor of 2 uncertainty is a realistic estimate of the accuracy with which cluster X-ray luminosities can be predicted with the present generation of techniques and computing resources.

REFERENCES

Anninos, P., & Norman, M. L. 1996, ApJ, 459, 12
Balsara, D. S. 1995, J. Comput. Phys., 121, 357
Bardeen, J. M., Bond, J. R., Kaiser, N., & Szalay, A. S. 1986, ApJ, 304, 15
Bartelmann, M., & Steinmetz, M. 1996, MNRAS, 283, 421
Bertschinger, E. 1985, ApJS, 58, 39
Berger, M. J., & Colella, P. 1989, J. Comput. Phys, 82, 64
Bode, P. W., Xu, G., & Cen, R. 1996, in Supercomputing '96, CD-ROM (New York: IEEE)[25]
Bond, J. R., & Myers, S. 1996, ApJS, 103, 1
Boris, J. P., & Book, D. L. 1973, J. Comput. Phys., 11, 38
———. 1976, J. Comput. Phys., 20, 397

Bryan, G. L., Cen, R., Norman, M. L., Ostriker, J. P., & Stone, J. M. 1994, ApJ, 428, 405
Bryan, G. L., Norman, M. L., Stone J. M., Cen, R., & Ostriker, J. P. 1995, Comput. Phys. Comm., 89, 149
Bryan, G. L., & Norman, M. L. 1995, BAAS, 187, 9504
———. 1999, in preparation
Cen, R. 1992, ApJS, 78, 341
Cen, R. Liu, F., Jameson, A., & Ostriker J. P. 1990, ApJ, 362, L41
Cen, R., & Ostriker J. P. 1994, ApJ, 429, 4
Couchman, H. M. P., Pearce, F. R., & Thomas, P. A. 1996, preprint (astro-ph 9603116)
Couchman, H. M. P., Thomas, P. A., & Pearce, F. R. 1995, ApJ, 452, 797
Efstathiou, G., Bond, R. J., & White, S. D. M. 1992, MNRAS, 258, 1p
Efstathiou, G., & Eastwood, J. W. 1981, MNRAS, 194, 503
Evrard, A. E. 1988, MNRAS, 235, 911
———. 1990, ApJ, 363, 349

[25] Available over the Internet at http://www.physics.upenn.edu/bode/SC96/INDEX.HTM.

Gingold, R. A., & Monaghan, J. J. 1977, MNRAS, 181, 375
Gnedin, N. Y. 1995, ApJS, 97, 231
Gnedin, N. Y., & Bertschinger, E. 1996, ApJ, 470, 115
Harten, A. 1983, J. Comput. Phys., 49, 357
Hoffman, Y., & Ribak, E. 1991, ApJ, 380, L5
Huss, A., Jain, B., & Steinmetz, M. 1999, MNRAS, in press
Kang, H., Cen, R., Ostriker, J. P., & Ryu, D. 1994a, ApJ, 428, 1
Kang, H., Ostriker, J. P., Cen, R., Ryu, D., Hernquist, L., Evrard, A. E.,
    Bryan, G., & Norman, M. L. 1994b, ApJ, 430, 83
Kates, R. E., Kotok, N., & Klypin, A. A. 1990, A&A, 243, 295
Klypin, A. A., Kates, R. E., & Khokhlov, A. 1992, in New Insights into the
    Universe, ed. V. Martínez, M. Portilla, & D. Saez, Lecture Notes in
    Physics 408 (Berlin: Springer), 171
Lucy, L. 1977, AJ, 82, 1013
Mohr, J. J., & Evrard, A. E. 1997, ApJ, 491, 38
Navarro, J. F., Frenk, C. S., & White, S. D. M. 1995, MNRAS, 275, 720
———. 1997, ApJ, 490, 493
Navarro, J. F., & White, S. D. M. 1993, MNRAS, 267, 401
Oran, E. S., & Boris, J. P. 1986, Numerical Simulation of Reactive Flow
    (New York: Elsevier)
Owen, J. M., Villumsen, J. V., Shapiro, P. R., & Martel, H. 1998, ApJS, 116,
    155
Pearce, F. R., & Couchman, H. M. P. 1997, NewA, 2, 411 (PC 97)
Pen, U.-L. 1995, ApJS, 100, 269
———. 1998, ApJS, 115, 19
Porter, D. 1985, Ph.D. thesis, Univ. California, Berkeley
Ryu, D., Ostriker, J. P., Kang, H., & Cen, R. 1993, ApJ, 414, 1

Shapiro, P. R., Martel, H., Villumsen, J. V., & Owen, J. M. 1996, ApJS, 103,
    269
Steinmetz, M. 1996, MNRAS, 278, 1005
Steinmetz, M., & Müller, E. 1993, A&A, 268, 391
Sugimoto, D., Chikada, Y., Makino, J., Ito, T., Ebisuzaki, T., & Umemura,
    M. 1990, Nature, 345, 33
Wadsley, J. W., & Bond, J. R. 1997, in ASP Conf. Ser. 123, Computational
    Astrophysics, Proc. 12th Kingston Meeting, ed. D. Clarke & M. West
    (San Francisco: ASP), 332
Warren, M. S., & Salmon, J. K. 1993, in Supercomputing '93 (Los Ala-
    mitos, CA: IEEE Comput. Soc.), 12[26]
———. 1995, Comput. Phys. Commun., 87, 266
White, S. D. M. 1996, in Cosmology and Large-Scale Structure, ed.
    R. Schaefer, J. Silk, M. Spiro, & J. Zinn-Justin (Dordrecht: Elsevier), 127
White, S. D. M., Navarro, J. F., Evrard, A. E., & Frenk, C. S. 1993, Nature,
    366, 429
Yepes, G., Kates, R., Klypin, A., & Khokhlov, A. 1995, in Clustering in the
    Universe, Proc. XXX Rencontres des Moriond, ed. S. Maurogordato
    (Gif-sur-Yvette: Editions Frontières), 209
———. 1996, in ASP Conf. Ser. 94, Measuring and Modelling the Uni-
    verse, Proc. UIPM-ECN Conf., ed. M. J. Pons, V. Martínez, & P. Coles
    (San Francisco: ASP), 125

[26] Also available over the Internet as at http://qso.lanl.gov/papers/
sc93/reprint.ps.